Manuscript submitted to **Biophysical** *Journal*
Article

Time-resolved fluorescence anisotropy and molecular dynamics analysis of a novel GFP homo-FRET dimer

Yurema Teijeiro-Gonzalez[1], Alessandro Crnjar[1], Andrew J. Beavil[2], Rebecca L. Beavil[2], Jakub Nedbal[1], Alix Le Marois[3], Carla Molteni[1], and Klaus Suhling[1]

[1]Department of Physics, King's College London, Strand, London WC2R 2LS, UK
[2]Randall Centre for Cell and Molecular Biophysics, King's College London, New Hunt's House, Guy's Campus, London SE1 1UL, UK
[3]Department of Cell Biology, The Francis Crick Institute, 1 Midland Rd, London NW1 1ST, UK
[*]Correspondence: yurema.teijeiro_gonzalez@kcl.ac.uk

ABSTRACT Förster resonance energy transfer (FRET) is a powerful tool to investigate the interaction between proteins in living cells. Fluorescence proteins, such as the green fluorescent protein (GFP) and its derivatives, are co-expressed in cells linked to proteins of interest. Time-resolved fluorescence anisotropy is a popular tool to study homo-FRET of fluorescent proteins as an indicator of dimerisation, where its signature consists of a very short component at the beginning of the anisotropy decay. In this work we present an approach to study GFP homo-FRET via combination of time-resolved fluorescence anisotropy, the stretched exponential decay model and molecular dynamics (MD) simulations. We characterise a new FRET standard formed by two enhanced GFPs (eGFPs) and a flexible linker of 15 aminoacids (eGFP15eGFP) with this protocol, which is validated by using an eGFP monomer as a reference. An excellent agreement is found between the FRET efficiency calculated from the fit of the eGFP15eGFP fluorescence anisotropy decays with a stretched exponential decay model ($\langle E^{exp}_{FRET} \rangle = 0.25 \pm 0.05$) and those calculated from the MD simulations ($\langle E^{MD}_{FRET} \rangle = 0.18 \pm 0.14$). The relative dipole orientation between the GFPs is best described by the orientational-factors $\langle \kappa^2 \rangle = 0.17 \pm 0.16$ and $\langle |\kappa| \rangle = 0.35 \pm 0.20$, contextualised within a static framework, where the linker hinders the free rotation of the fluorophores and excludes certain configurations. The combination of time and polarisation-resolved fluorescence spectroscopy with molecular dynamics simulations is shown to be a powerful tool for the study and interpretation of homo-FRET.

SIGNIFICANCE A new FRET standard based on a GFP dimer is described, useful for reference when investigating homo-FRET in cells, e.g. when studying protein dimerisation, or when using homo-FRET based biosensors. Since FRET depends on the donor and acceptor fluorophore separation and orientation, its heterogeneity for the GFP dimer may yield a multi-exponential time-resolved fluorescence anisotropy decay. For this reason, we explore the stretched exponential decay model to interpret time-resolved fluorescence anisotropy decay data. With it and the support of molecular dynamics simulations, we are able to calculate the distribution of orientation factor κ (and κ^2) and the range of distances of the two GFP fluorophores, crucial for accurately processing the experimental data.

INTRODUCTION

The green fluorescent protein (GFP) was first extracted and purified from the jellyfish *Aequorea victoria*, whose discovery and development led to the Chemistry Nobel Prize in 2008(1). X-ray crystallography studies revealed that GFP (27 kDa, made of 238 aminoacids) is a barrel-shaped protein, with a length of 4.2 nm and diameter of 2.4 nm(2, 3). The fluorophore of the protein lies at the centre of the structure, where 4 aminoacids are responsible for the fluorescence emission. The complex photophysics of this protein and its variants have been widely studied, and protonated and deprotonated absorption bands have been identified(4–8). Nowadays, this protein and its genetically encoded variants are extensively used in many biological applications, e.g. fluorescence microscopy to image cells, monitor gene expression, act as sensors for calcium, copper or other ions, locate proteins, study their interactions and describe their dynamics(9, 10).

The fluorescence decay of GFP is sensitive to the refractive index of its environment(11), which can be exploited in fluorescence lifetime imaging (FLIM) to map environmental changes associated with the refractive index such as protein

concentration.(12, 13) The combination of GFP and its spectral variants in donor and acceptor pairs for Förster Resonance Energy Transfer (FRET) allows the detection of protein interaction(14) via the donor's fluorescence decay. In addition, biosensors have been designed according to this principle: For example, in the calmodulin calcium sensor cameleon, Ca^{2+} ions bind to the structure and induce a conformational change which is identified via FRET between a cyan and yellow fluorescent protein(15, 16).

Polarisation-resolved fluorescence lifetime measurements allow time-resolved fluorescence anisotropy studies. In fluorescence anisotropy studies, the rotational mobility of the fluorophore is described by the rotational correlation time, which accounts for the time it takes the fluorophore to rotate by 1 radian(17). This property is sensitive to viscosity(18), which can be imaged via time-resolved fluorescence anisotropy imaging (tr-FAIM).(19)

Due to its small Stokes shift and significant overlap of absorption and emission spectra, GFP is an ideal candidate for homo-FRET, an energy transfer phenomenon where donor and acceptor are identical. The GFP Förster distance R_0, i.e. the distance at which the FRET efficiency is 50%, was reported as 4.65 nm ± 0.09 nm(20). Moreover, due to GFP's large volume, its Brownian rotational diffusion is slow compared to its excited state lifetime, and it is clearly distinguishable from fast FRET. In addition, a GFP fluorescence quantum yield of 0.6 and peak extinction coefficient of 55,900 M^{-1} cm^{-1} (1, 10) make GFP and its derivatives highly suitable for homo-FRET studies - much more so than small organic dyes, as their fast rotational Brownian motion in fluid environments obscures homo-FRET. When FRET occurs among identical proteins in homo-FRET pairs, the transfer of non-radiative energy of one protein to the other is a reversible process. The transfer rate constants in both directions are identical if the fluorophores are in the same environment. This leads to no change in the overall emission spectrum and fluorescence lifetime(17), which is the reason why FLIM cannot be employed to study homo-FRET for GFP. Conversely, time-resolved fluorescence anisotropy can detect FRET between identical fluorescent proteins. In fact, this technique has been used in living cells to study the effect of protein dimerisation and aggregation on the cell functioning(19, 21–23). While oligomerisation in the biological milieu may involve a mixture of monomers and dimers as well as higher order oligomers, at various distances and orientations, and does not typically involve a covalent linker, the short FRET component in the anisotropy decay is a qualitative tell-tale sign of the occurrence of oligomerisation. The advantage of this approach is that it can be established with a single type of fluorescence label, emitting in a single well-defined spectral region, and no two-colour labelling for hetero-FRET is needed.

Several hetero-FRET constructs - where donor and acceptor are not identical - have been described and established as FRET standards (24, 25). Unlike homo-FRET, hetero-FRET is an irreversible transfer of excited state energy from the donor to the acceptor. Since it represents a de-excitation pathway for the donor, it shortens the donor decay, and it can thus be studied by observing the fluorescence decay of the donor. This is best done via time-correlated single photon counting (TCSPC), as this approach provides the lowest experimental uncertainty in the FRET efficiency (26). For example, Matthews et al. (24) investigated the fluorescence lifetime of dimers of eGFP and the monomeric red fluorescent protein 1 (mRFP1) with different linker-lengths, where eGFP and mRFP1 were donor and acceptor, respectively. They proved that when the linker length was shorter, FRET between proteins increased, yielding a decrease of the donor fluorescence lifetime and acceptor anisotropy(24). Likewise, in the work by Koushik et al., Cerulean, Venus and $Venus_{Y67C}$ constructs were investigated using fluorescence lifetime measurements, sensitised acceptor emission and spectral imaging: their results presented an excellent agreement(25). The unique characterisation of these constructs enabled their introduction as FRET standards.

In order to establish FRET standards for homo-FRET studies, parameters other than the fluorescence lifetime must be employed. One example is the combination of fluorescence polarisation and fluctuation analysis (FPFA) developed in Vogel's group to study homo-FRET in Venus FRET constructs(27).

Single and double exponential decay models are extensively used for the interpretation of the time-resolved fluorescence anisotropy decays in the presence of FRET(28–30). However, due to its apparent more complicated form, very little has been reported on the application of the stretched exponential decay model as a FRET indicator(31, 32). Here, we present a new anisotropy FRET standard formed by two eGFPs tethered by a linker of 15 aminoacids (eGFP15eGFP), and describe a new protocol based on the combination of the stretched exponential decay model and molecular dynamics (MD) simulations as a tool to study homo-FRET.

MATERIALS AND METHODS

Sample preparation

eGFP is a mutant of the wild-type GFP, with mutations of serine to threonine at position 65 (S65T) and phenylalanine to leucine at position 64 (P64L). DNA for double eGFP with a $(GGGGS)_3$ linker, where G refers to glycine and S to serine, was synthesised as a double stranded DNA gBlock (Integrated DNA Technologies), and cloned into pET151 according to manufacturer's instructions (ThermoFisher). eGFP alone was also cloned into pET151. This vector adds an N-terminal 6xHis and V5 tag, and a

TEV cleavage site, giving an extra 33 amino acids on the N-terminus of the protein. The constructs and mutations were verified by sequencing (Eurofins Genomics). Both eGFP constructs were provided by the Protein Production Facility of King's College London. For expression, the constructs were transformed into BL21 Star (DE3) *E. coli* (ThermoFisher). Colonies were used to inoculate a starter culture in Luria broth containing 100 μg/ml ampicillin, and left shaking at 37°C for 5 hours. This was used to inoculate 100 ml ZYP-5052 autoinduction media (33) and the culture grown at 18°C shaking for 65 hours. The bacteria were harvested by centrifugation at 4000 g and frozen at -80°C. Pellets were thawed and EDTA Complete protease inhibitor tablets added (Roche) then the *E. coli* were lysed using BugBuster (Merck Millipore) according to the manufacturer's instructions. The protein was found in the soluble fraction and was purified by passing over a 1 ml Histrap ff crude column (GE Healthcare) using a Biorad NGC system. The column was washed with 30 column volumes of 10 mM sodium phosphate, 500 mM NaCl, 20 mM imidazole pH 7.4 and the bound protein eluted with 10 mM sodium phosphate, 500 mM NaCl, 500 mM imidazole pH 7.4. Fractions containing proteins were then pooled and concentrated (Amicon Ultra 15, Merck Millipore), then further purified using size exclusion chromatography. Using a Gilson HPLC system, samples were run on a Superdex 200 increase 10/300 GL column in phosphate buffered saline (PBS) at pH 7.4 (OXOID). Fractions corresponding to monomer for each construct were pooled, and concentrated as required, resulting in different amounts of stock solution for GFP monomer and GFP dimer. For the measurements, the concentrations $[C]$ for monomer and dimer were $[C]_{monomer}$ = 0.89 μM and $[C]_{dimer}$ = 0.34 μM, respectively, in 0%, 5%, 10%, 15%, 20%, 25%, 30% and 35%, 45% and 50% (v/v) glycerol in PBS solutions. This corresponds to an average nearest neighbour distance d = 57 nm between the GFP monomers, and d = 79 nm between the dimers, with $d = 0.55/[C]^{1/3}$, with $[C]$ quoted in fluorophores per volume (34, 35). With an average decay time τ of 2.6 ns, the diffusion length l, i.e. the average distance travelled in the excited state, given by $l = \sqrt{6D\tau}$, with D the diffusion coefficient ($D_{GFP} = 0.87 \times 10^{-10} m^2/s$ (36)) is l = 1.2 nm. This is much shorter than the nearest neighbour distance, and interaction between the constructs is thus insignificant at the concentrations used in this work.

Steady-State Spectra

Steady-state polarisation-resolved excitation and emission spectra were obtained on a luminescence spectrometer (Perkin-Elmer LS-5) using a 1 cm pathlength quartz cuvette. Four measurements were taken per experiment using two polarisers, one located between the excitation source and the sample and the second between the sample and the emission detector: $I_{VV}(\lambda)$, $I_{VH}(\lambda)$, $I_{HH}(\lambda)$ and $I_{HV}(\lambda)$, where subscript V refers to the vertical and H to the horizontal polarisation for excitation and emission, respectively. Measurements were taken from λ_{exc} = 350 nm to λ_{exc} = 520 nm, in 2 nm steps. Fluorescence emission was detected at 530 nm. The data analysis was carried out as described previously, taking into account the spectral sensitivity of the spectrometer(37). The emission spectrum was recorded on the same setup without polarisers. The excitation wavelength was λ_{exc} = 450 nm. Fluorescence emission was detected from λ = 460 nm to λ = 660 nm, every 2 nm.

The absorption spectrum was obtained by using an absorption spectrometer (Hitachi U-4100 dual beam spectrometer), with a 1 cm pathlength quartz cuvette. The absorption spectrum was recorded from 330 to 560 nm in 2 nm steps and the solvent (buffer) absorption spectrum was subtracted. The spectral overlap $J(\lambda)$ between the absorption and emission spectra was calculated via the a|e - UV-Vis-IR Spectral Software(38), where the GFP peak extinction coefficient at 488 nm, ϵ_{488} = 55,900 $M^{-1}cm^{-1}$, was introduced as an input(10).

Time-resolved fluorescence anisotropy measurements

Single fluorescence decays were measured on an inverted confocal microscope (Leica TCS SP2). Excitation was provided by a 467 nm diode laser (Hamamatsu PLP-10 470) at a repetition rate of 20 MHz with an average power in the microwatt region. Time-resolved fluorescence anisotropy experiments were performed with two TCSPC (Time-Correlated Single Photon Counting) cards (SPC-150 Becker & Hickl) connected to two hybrid detectors (Becker & Hickl HPM-100-40). Fluorescence emission, passed through a 514/30 bandpass filter, was separated into two orthogonal polarisation components by a polarising beam splitter cube (Edmund Optics) before reaching the hybrid detectors. The acquisition time was 5 minutes and the TCSPC time resolution was 4096 bins of 12 ps each. We calculated the fluorescence anisotropy decays and also the fluorescence decays from these measurements. In addition, the fluorescence lifetime measurements were performed without polarising beam splitter cube and using a single detector and one TCSPC card only for solutions up to 30% glycerol. A sample volume of 250 μl was measured in a 8-well coverslip-bottom plate (ibidi) at room temperature. The schematic of the setup is presented in Figure 1.

Refractive index measurements

The refractive index was measured using an Abbe refractometer at room temperature. A tungsten lamp (visible range) was used and the system was calibrated with water, whose value is very well known (n = 1.336 at λ = 589 nm and T = 20°C)(39). Three readings were averaged per measurement.

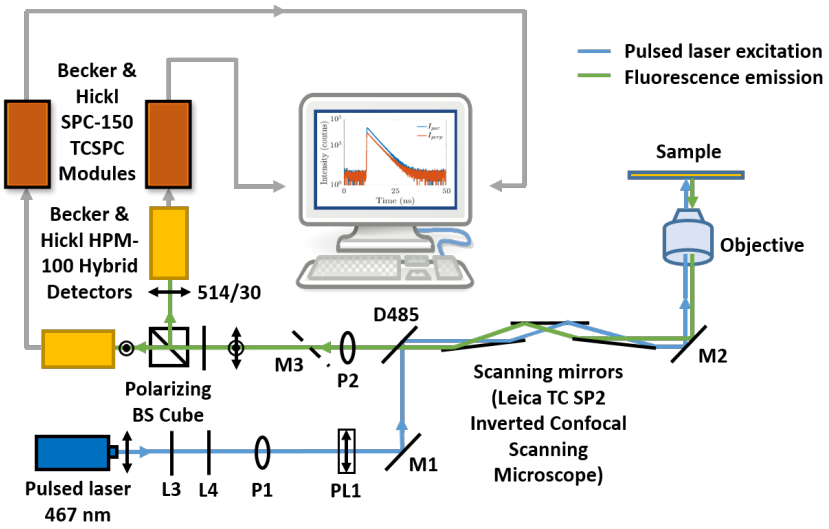

Figure 1: Schematic of the experimental setup. M stands for mirror, L for lens, P for pinhole, D for dichroic and PL for polariser.

Molecular dynamics simulations

The model of the GFP monomer was created from a X-ray structure solved at 0.19 nm resolution (protein data bank entry: 1GFL)(3). The internal fluorophore was taken from the eGFP protein data bank entry 2Y0G(40) and inserted in the homologous GFP model using the software Yasara(41). To build the GFP15GFP dimer, we duplicated the monomer structure, and translated the copy so that the two monomers were separated from each other by about 2 nm. This two-domain template was then uploaded in the modelling server SWISS-MODEL(42–46) to build a linker of sequence GGGGSGGGGSGGGGS. The resulting structure of this linker was characterised by a certain degree of folding due to the distance between the two monomers. Both the monomer and the dimer were solvated with a 1.2 nm water buffer in a truncated octahedral periodically repeated supercell. Na^+ ions were added to neutralise the charge of the system, as each monomer contains 21 negative charges. Overall, the monomer system contains 29,922 atoms while the dimer system contains 123,999 atoms. Simulations were performed with the wild-type GFP, while the experiments were carried out using eGFP with a cleavable HIS-tag. The structure of these types of GFP is identical, only the fluorophores are slightly different, and we do not expect the Brownian rotation of the protein to be affected by this distinction.

The AMBER ff14sb force-field(47) was used for both the monomer and the dimer. The internal fluorophore was parametrised with the General AMBER force field, and its partial charges were assigned according to the AM1-BCC charge scheme(48, 49). As in previous simulation studies of fluorescence anisotropy(50), it was assumed that the ground state interaction potential can also be representative of the excited states. The proteins were solvated in water, which has a similar viscosity to PBS, used in the experiment. The commonly used TIP3P(51) water model was chosen. The low value of the viscosity of this water model with respect to experiments(52, 53) was taken into account by a suitable rescaling procedure when calculating rotational correlation times, as described in the Results section. The rotational correlation time is related to the solution viscosity via the Stokes-Einstein-Debye relationship(17):

$$\theta = \frac{\eta V}{k_B T} \tag{1}$$

where k_B is the Boltzmann constant, T the absolute temperature, η the environmental viscosity and V is the volume of the fluorophore.

Molecular dynamics simulations of the GFP monomer and dimer were carried out with AMBER 12 (PMEMD)(54). The SHAKE algorithm was used to restrain bonds containing hydrogens, and a time step of 2 fs was used (except that for the NPT equilibration, for which a time step of 1 fs was used), and a cutoff of 1 nm was used for the non-bonded interactions. Long-range electrostatic interactions were evaluated with Particle Mesh Ewald. The system was first minimised by restraining the protein with a harmonic potential of spring constant 10^3 kcal mol^{-1} nm^{-2} and then without any restraint. It was then heated in the canonical (NVT) ensemble for 1 ns (0.5 ns in the case of the monomer) from 0 to 300 K by means of the weak-coupling Berendsen algorithm with a time constant of 0.5 ps(55), keeping the protein restrained. It was equilibrated at 1 bar in an isothermal-isobaric (NPT) ensemble for 5 ns (2 ns in the case of the monomer) by means of a Langevin thermostat with collision frequency of 2.0 ps^{-1} and a Berendsen barostat with time constant of 0.5 ps. Finally, a production of 500 ns in the

microcanonical (NVE) ensemble was carried out. The NVE ensemble was chosen as it is does not disrupt diffusion processes, such as the the rotational diffusion we are interested in.

The fluorescence anisotropy decay can be represented by the auto-correlation function (ACF) of the normalised transition dipole moment direction(50, 56–59), which is defined as a single unit vector for each fluorophore. There is one for the monomer, and two for the dimer(50); in the latter case the anisotropy is calculated as the average of the anisotropies of each of the two monomers.

The fluorescence anisotropy decay of a rotating unit is given by the following expression:

$$r(t) = \frac{2}{5}\left\langle \frac{3(\vec{\mu}(t_0)\cdot\vec{\mu}(t_0+t))^2}{2} - \frac{1}{2}\right\rangle_{t_0} \tag{2}$$

where $\vec{\mu}(t)$ is a given normalised transition dipole moment as a function of time, and the brackets indicate an average over every possible initial time t_0. A discreet version of equation 2, that can be implemented for the post-production of an MD simulation trajectory, is given by:

$$r(t_i) \approx \frac{2}{5}\frac{1}{T_{tot}-t_i}\sum_{t'_j=0}^{T_{tot}-1-t_i}\frac{3(\vec{\mu}(t'_j)\cdot\vec{\mu}(t'_j+t_i))^2-1}{2} \tag{3}$$

where t_i and t'_j are the i-th and j-th time steps respectively, and T_{tot} is equal to the number of time steps in the MD trajectory. In the case of GFP, $\vec{\mu}$ can be defined as the normalised average of the vector connecting atoms C^6 and O^5, and the one connecting atoms C^3 and N^1 in the fluorophore (as shown in Figure 2 a)(60, 61).

Under the assumption of ergodicity, we divided the 500 ns-long trajectories into 10 trajectories of 50 ns each. The ACF, with a time resolution of 10 ps, was then computed on the last 9 and averaged, while the first was discarded for equilibration reasons. This way of dividing the trajectory was chosen to provide large enough statistics for averaging the ACF, while at the same time providing a long enough time window for the average ACF to be fitted over.

From the MD trajectories, the FRET orientation factor κ^2 is calculated as(60):

$$\kappa^2 = ((\vec{D}\cdot\vec{A}) - 3(\vec{D}\cdot\vec{R})(\vec{A}\cdot\vec{R}))^2 \tag{4}$$

where $\vec{D}$ and $\vec{A}$ are the normalised transition dipole moments of the donor and acceptor fluorophores, respectively, and $\vec{R}$ is the normalised distance vector between the two fluorophores. Here this was calculated as the average of the four vectors linking the coordinates of four atoms in the donor fluorophore (the surrogate GFP benzylidene C^1 and C^2 and imidazolone N^3 and C^4) with their corresponding ones within the acceptor fluorophore, as shown in Figure 2 a (60).

Equation 4 can be rewritten as a function of the angle between vectors:

$$\kappa^2 = (\cos\alpha_T - 3\cos\alpha_D\cos\alpha_A)^2 \tag{5}$$

where α_T, α_D and α_A are the angles between $\vec{D}$ and $\vec{A}$, $\vec{D}$ and $\vec{R}$, and $\vec{A}$ and $\vec{R}$, respectively.

The FRET efficiency was calculated from the relative dipole orientation between the two GFPs through κ^2 and their separation R as(17):

$$E_{FRET} = \frac{1}{\left(\frac{R}{R_0}\right)^6+1} \tag{6}$$

where R_0 contains κ^2 and is the so-called Förster distance at which the energy efficiency due to FRET is half. It is given by(17):

$$R_0 = 0.021(\kappa^2 n^{-4}\Phi J(\lambda))^{\frac{1}{6}}\,[\text{nm}] \tag{7}$$

where Φ is the quantum yield of the donor in the absence of the acceptor, n is the refractive index of the environment where the FRET takes place and $J(\lambda)$ is the overlap integral of the absorption spectrum of the acceptor and the emission spectrum of the donor.

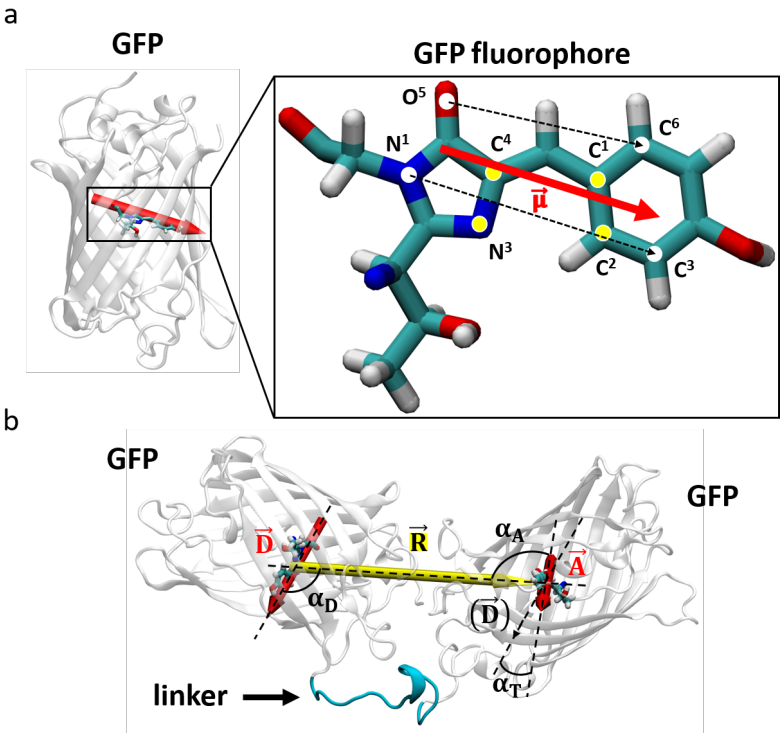

Figure 2: Illustration of the GFP15GFP dimer configuration and the linker. (a) The fluorophore responsible for the fluorescence emission is shown in the enlarged image, where the atoms used for defining the transition dipole moment and the distance between proteins are indicated. The transition dipole moment $\vec{\mu}$ is represented as a red arrow, and its direction is that of the average of the two vectors that link atoms C^6-O^5 and C^3-N^1 (dashed black arrows). (b) Representative GFP15GFP configuration. Donor ($\vec{D}$) and acceptor ($\vec{A}$) transition dipole vectors are shown in red. The distance $\vec{R}$ between the fluorophores is shown in yellow (while the four atoms whose centre of mass is used for each of the two ends of $\vec{R}$ are shown in yellow in the enlarged image in (a)). The angles between the vectors are α_D (between $\vec{D}$ and $\vec{R}$), α_A (between $\vec{A}$ and $\vec{R}$) and α_T (between $\vec{D}$ and $\vec{A}$). The flexible linker that connects the two GFPs is shown in blue.

Data analysis

The parallel and perpendicular fluorescence intensity decays, $I_{\parallel}(t)$ and $I_{\perp}(t)$ respectively, were used to produce the experimental time-resolved fluorescence anisotropy decay using the following equation(17):

$$r(t) = \frac{I_{\parallel}(t) - GI_{\perp}(t)}{I_{\parallel}(t) + 2GI_{\perp}(t)} \tag{8}$$

where G corresponds to the efficiency ratio between detection paths.

The fluorescence anisotropy decay of monomeric eGFP was fitted with a single exponential decay model:

$$r(t) = r_0 e^{-t/\theta} \tag{9}$$

where r_0 is the initial anisotropy and θ is the rotational correlation time(17). The eGFP15eGFP fluorescence anisotropy decay was fitted with double(28–30) and stretched exponential(32, 62) decay models. The stretched exponential decay model was given by the following expression, in the static regime where the donor's fluorescence decay in the presence of an acceptor is much shorter than its rotational rate:

$$r(t) = r_0 e^{-\gamma_{st} t^{\delta}} \tag{10}$$

where δ is the dimensionality of the system. If the system is 3-dimensional, then $\delta = 1/2$, and for 2 dimensions, $\delta = 1/3$. (31, 63)

γ_{st} is given by:

$$\gamma_{st} = \sqrt{\frac{\pi}{2\tau}} c \left(\frac{3}{2}\right)^{1/2} \langle |\kappa| \rangle \tag{11}$$

where $\langle|\kappa|\rangle$ accounts for the mean of the absolute value of the orientational-factor κ, τ is the fluorescence lifetime of the donor in the absence of any acceptor and c is a dimensionless parameter that accounts for the number of fluorophores within a space of radius R_0.

The FRET energy efficiency, calculated from the application of the stretched exponential decay model to the anisotropy decay, is given by(32, 64, 65):

$$E_{FRET} = \sqrt{\pi} y e^{y^2} [1 - \mathrm{erf(y)}] \tag{12}$$

where $y = \frac{\sqrt{\tau}}{2}\gamma_{st}$ and erf is the error function.

Additional information about the derivation and relationship between parameters of the stretched exponential decay model is provided in the Supplementary Material.

An alternative model to interpret the eGFP15eGFP anisotropy decay is the double exponential function, where one component accounts for rotational motion, and one component accounts for homo-FRET:

$$r(t) = r_{01} e^{-t/\theta} + r_{02} e^{-t/\phi} \tag{13}$$

where θ is the rotational correlation time, ϕ the inverse FRET rate constant and r_{01} and r_{02} the initial anisotropy.

For a homo-FRET dimer, the single-step energy transfer rate k_T occurs in both ways identically. For this reason, the relationship between ϕ and k_T is given by $k_T = 1/2\phi$(22, 66). Knowing this relationship and that k_T depends on the sixth-power of the separation between fluorophores R ($k_T = \tau^{-1}(R_0/R)^6$(64)), equation 6 can be rewritten as follows:

$$E_{FRET} = \frac{k_T}{\tau^{-1} + k_T} \tag{14}$$

where τ is the fluorescence lifetime of the isolated donor, i.e. the average time it takes for the excited fluorophore to return to its ground state.

In order to obtain the FRET efficiency using equation 14, the average fluorescence lifetime of the monomeric eGFP was calculated from the denominator of equation 8 ($I(t) = I_{\parallel}(t) + 2GI_{\perp}(t)$) and fitted with a double exponential decay model, which was convoluted with the instrument response function (IRF)(17, 67):

$$I(t) = IRF \circledast (A_1 e^{-t/\tau_1} + A_2 e^{-t/\tau_2}) \tag{15}$$

where A_i corresponds to the fluorescence intensity contribution of each fluorescence lifetime τ_i.

The intensity-averaged lifetime τ_{avg} was calculated as(68):

$$\tau_{avg} = \frac{A_1\tau_1^2 + A_2\tau_2^2}{A_1\tau_1 + A_2\tau_2} \tag{16}$$

The dependence of the average eGFP and eGFP15eGFP fluorescence lifetime on its environmental refractive index was assessed using the Strickler-Berg formula(69):

$$k_r = 2.88 \times 10^{-9} n^2 \frac{\int F(\tilde{\nu}) d\tilde{\nu}}{\int F(\tilde{\nu}) \tilde{\nu}^{-3} d\tilde{\nu}} \int \frac{\epsilon(\tilde{\nu}) d\tilde{\nu}}{\tilde{\nu}} \tag{17}$$

where k_r is the radiative rate constant and is related to the fluorescence lifetime τ and the non-radiative rate constant k_{nr} by $\tau = \frac{1}{k_r + k_{nr}}$. F is the fluorescence emission, ϵ the extinction coefficient and $\tilde{\nu}$ is the wavenumber ($\tilde{\nu} = \frac{1}{\lambda}$, with λ wavelength).

Fluorescence decays were analysed and plotted with a home-built MATLAB script, where the Levenberg-Marquardt algorithm was employed to fit the data via the non-linear least squares method.

The viscosity of each solution was calculated by the method developed by Nian-Sheng Cheng(70), which takes into account the water/glycerol ratio of the solution and its temperature.

Simulated fluorescence anisotropy decays calculated from an autocorrelation function were fitted with a single exponential decay model equation 9 and hindered rotation decay model

$$r(t) = (r_0 - r_\infty) e^{-t/\theta} + r_\infty \tag{18}$$

where r_∞ accounts for a hindered rotation)(17), for GFP and GFP15GFP, respectively. The ratio $\frac{r_\infty}{r_0}$ can be used to calculate the semicone angle θ_c in the wobble-in-a-cone model (71, 72)

$$\frac{r_\infty}{r_0} = \frac{1}{2} cos\theta_c (1 + cos\theta_c) \tag{19}$$

From the rotational correlation time, the solution viscosity was calculated using the Stokes-Debye-Einstein relationship (equation 1).

The trajectories post-production were analysed with MDAnalysis (73, 74) and CPPTRAJ (75). VMD was used for visualising the trajectories(76). All simulated data were plotted in MATLAB and, similarly to the experimental data, the fits were performed using the non-linear least squares method and the Levenberg-Marquardt algorithm.

RESULTS AND DISCUSSION

Red-edge excitation of eGFP15eGFP confirms homo-FRET

Figure 3 a shows the absorption and emission spectra of eGFP in PBS. The overlap spectrum $J(\lambda)$ in equation 7 was calculated to be $J(\lambda)$=8.7 $\times$ 10^{14} $M^{-1}cm^{-1}nm^4$. Using the static random average κ^2 of 0.69^2, a quantum yield Φ=0.6 and refractive index n=1.336, we obtain a Förster radius R_0 for GFP-GFP homo-FRET of 4.34 nm from the spectra, and with κ^2=2/3, we obtain 4.59 nm, in excellent agreement with the 4.65 nm ± 0.09 nm quoted by (20), also using κ^2=2/3. Homo-FRET can be investigated by steady-state anisotropy at the red edge, where the fluorophore is excited with the lowest energy. At the red excitation edge, homo-FRET is suppressed. Steady-state anisotropy measurements of eGFP and eGFP15eGFP in PBS as a function of excitation wavelength are shown in Figure 3 b. The steady-state fluorescence anisotropy for monomer and dimer increased with the excitation wavelength. Both registered their lowest steady-state anisotropy values at lower excitation wavelengths in the ultra-violet region. The monomer featured higher steady-state anisotropy values compared to the dimer. This is consistent with the presence of homo-FRET for the dimer configuration, as homo-FRET provides an additional pathway for depolarisation after excitation, which results in lower anisotropy values. The anisotropy response reached is maximum for the monomer from 440 to 490 nm, while that corresponding to the eGFP dimer remained well below this, consistent with homo-FRET. The dimer anisotropy is rising towards longer wavelengths, and at the red-edge (~ 510-520 nm), it is the same as that of the monomer - which is an indication of suppression of homo-FRET due to red-edge excitation.

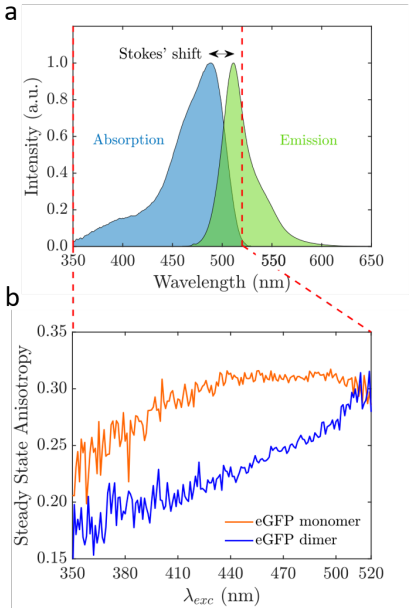

Figure 3: (a) Absorption and emission spectra of eGFP in PBS. (b) Steady-state anisotropy measurements at different excitation wavelengths for eGFP monomer and dimer in PBS.

The inverse average fluorescence lifetime of GFP monomer and dimer scale linearly with the refractive index of their environment

Fluorescence intensity decays were measured in a glycerol/PBS concentration range from 0% to 30% glycerol with a single detector, and fitted with a double exponential decay model, as a single exponential decay model did not fit well, in terms of residuals and χ_R^2 (χ_R^2>1.5). In Figure 4 a and b, two representative intensity decays for monomer and dimer solutions in 25% glycerol/PBS are presented. Two fluorescence lifetimes were determined for each of the samples: 2.04 ns (39%) and 2.77 ns (61%) for the eGFP monomer; 2.07 ns (44%) and 2.74 ns (56%) for the eGFP dimer. The percentages in brackets denote the fluorescence intensity contributions per fluorescence lifetime component. The χ_R^2 resultant from the fits were 1.17 and 1.07, respectively. Detailed data can be found in Supplementary Material (Table S1). The two fluorescence lifetimes determined in this work can be attributed to two different deprotonated excited states identified in the absorption spectrum(11, 77–79).

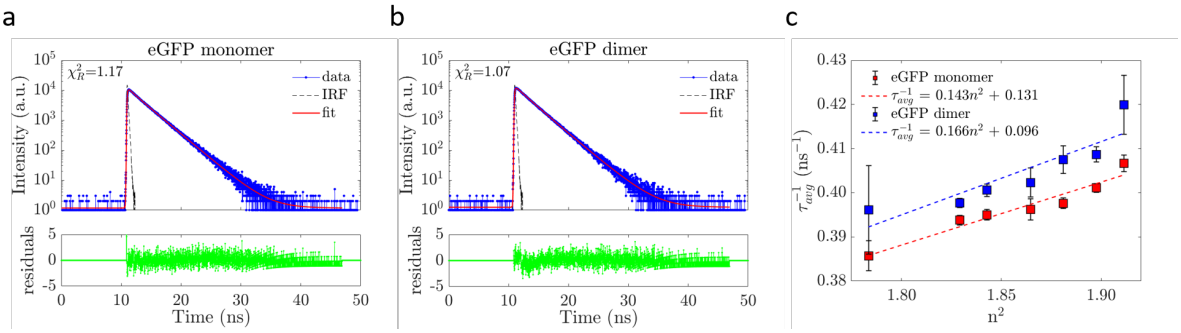

Figure 4: Representative fluorescence intensity decays for eGFP (a) monomer and (b) dimer in a PBS/glycerol solution with 25% glycerol. For each plot, the data is presented along with the IRF, fit and residuals. (c) A plot of the inverse average fluorescence lifetime against the square of the refractive index of the solution for GFP monomer and dimer. The data for both samples are fitted showing a linear relationship as established by the Strickler-Berg formula equation 17.

The Strickler-Berg formula was validated by plotting the reciprocal average fluorescence lifetime of each eGFP construct against the square of its environmental refractive index *n* (Figure 4 c). For both eGFP monomer and dimer and all the fractional solutions, the inverse average fluorescence lifetime was shown to scale linearly with the square of the refractive index. (80) (This is also the case for the individual lifetimes from the double exponential fit, as shown in Figure S13 in the SI, albeit with a larger experimental uncertainty.) This phenomenon has been used as a proxy for protein concentration when observed over the cell cycle (12, 13), and has shortened the GFP fluorescence decay of GFP-labelled transmembrane proteins compared to GFP-labelled proteins in the cytoplasm (81). This effect has also been used to study aerosol droplets (82).

The eGFP dimer fluorescence lifetime was slightly and consistently lower than the monomer fluorescence lifetime across the varying refractive index solutions. While the monomeric eGFP only probed the solvent surrounding it, the dimeric eGFP probed its surrounding solvent and the nearby eGFP monomer along with the linker. These have a higher refractive index than the solvent, yielding a slightly shorter GFP fluorescence decay. (80, 83)

Time-resolved fluorescence anisotropy measurements

eGFP monomer and dimer time-resolved fluorescence anisotropy decays

Time-resolved fluorescence anisotropy measurements were performed on eGFP dimers and eGFP monomers. Representative parallel and perpendicular fluorescence intensity decays for both monomeric eGFP and the dimer construct are displayed in Figure 5 a and b. Figure 5 c shows the time-resolved fluorescence anisotropy decays of the eGFP monomer in solutions of varying viscosity, and Figure 5 d shows the corresponding time-resolved fluorescence anisotropy for the dimer. As expected, the eGFP monomer time-resolved fluorescence anisotropy decays follow a single exponential decay model, depicted in Figure 6 a, as fluorescence depolarisation only occurs through Brownian rotational motion. For eGFP in PBS, we found a rotational correlation time of 16.46 ns ± 0.20 ns which agrees well with previous studies(18, 36, 60, 79, 84–91). As glycerol was added, the Brownian rotational motion slowed, and the rotational correlation time increased, up to 123 ns ± 6 ns in 50% glycerol. As the average fluorescence lifetime of eGFP is shorter than the rotational correlation time (and even decreases slightly as glycerol is added, see Figure 4 c and Table S1), it became increasingly difficult to measure it, and the experimental uncertainly of eGFP's rotational correlation time increased.

The eGFP dimer time-resolved fluorescence anisotropy decays were not appropriately fitted with a single exponential

decay model, as a very short component was identified at the beginning of the decay, a typical signature of homo-FRET between fluorescent proteins(27). In order to fit the eGFP dimer anisotropy data, two decay models were used: a double exponential (equation 13) and a stretched exponential (equation 10) (Figure 6 b and c). Both models assume that the protein configuration is isotropic and randomised, without any preferential orientation within the solution(29, 30, 32, 62) and $r_\infty = 0$. The double exponential decay model accounts for a slow Brownian rotational motion (with the rotational rate of the protein in the excited state much lower than the radiative and non-radiative de-excitation rates) and fast homo-FRET(29, 30). The stretched exponential decay model accounts for a distribution of rate constants for depolarisation (32, 62). The double exponential decay model has six free fitting parameters (background, shift, two pre-exponential factors, two decay times) whereas the stretched exponential only has five (background, shift, pre-exponential factor, dimensionality, stretched factor).

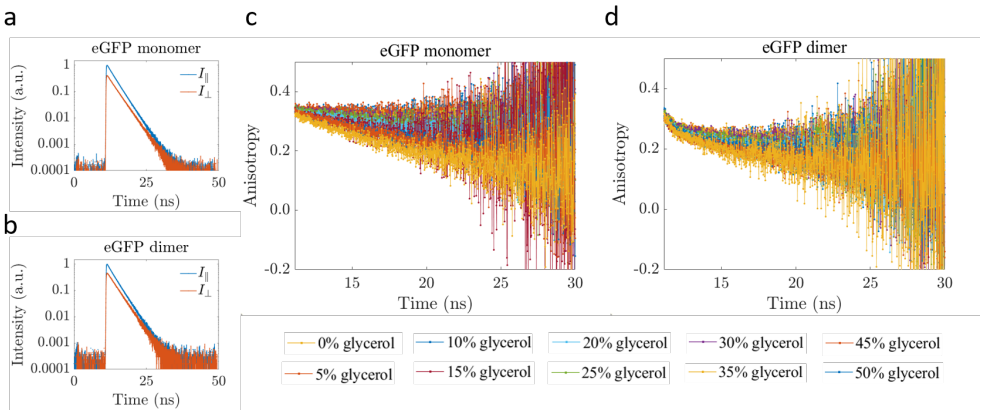

Figure 5: Representative parallel and perpendicular intensity decays for (a) eGFP monomer and (b) dimer. Time-resolved fluorescence anisotropy decays in different PBS/glycerol mixtures for (c) eGFP monomer and (d) eGFP dimer, with the glycerol content indicated.

The double exponential decay model fails to explain the eGFP dimer dynamics

The rotational correlation times calculated from the fit of the eGFP dimer anisotropy data with the double exponential decay model (equation 13) and in solutions of varying viscosities were compared with those from the eGFP monomer (Figure 6 d and Table S2). The rotational correlation times of the monomer (green squares) were plotted versus the solution viscosity and fitted with a straight line. The gradient is 18.1 ns/cP, and going through zero as demanded by equation 1. From the fit, the hydrodynamic radius of the eGFP was calculated: $R_h = 2.46$ nm ± 0.01 nm. This is in good agreement with values previously reported(92–95).

The rotational correlation times of the eGFP dimer were shown to follow a similar trend for low viscosity values, up to ~2 cP (Figure 6 d and Table S3), but then levelled off for viscosity values larger than 2 cP and showed an apparent lower rotational correlation time in comparison to the monomer (red data points). The shorter FRET inverse rate ϕ presented no correlation with viscosity (Figure 6 e). A shorter rotational correlation time of the dimer compared to the monomer would imply that the dimer rotates faster than the monomer in a solvent of the same viscosity. This is impossible as its radius of gyration is larger.

This means that the fit parameter associated with the long rotational correlation time appears to include a combination of Brownian rotational motion and FRET. The rotational correlation time of eGFP15eGFP should be larger than the corresponding one for the monomer - as shown by the MD simulations discussed below.

FRET efficiency heterogeneities between eGFPs can produce multi-exponential anisotropy decays

The logic used behind the application of the stretched exponential decay model lies in considering a distribution of distances and orientations between the FRET pairs. In the dynamic averaging regime where the rotational rate of the fluorophore in the excited state is much higher than its fluorescence decay rate, the average orientation per FRET pair is given by $\langle \kappa^2 \rangle$. However, here, for a fluorophore as large as GFP, $\langle |\kappa| \rangle$ determines the average orientation between the transition dipole moments of the donor and acceptor, when the system behaves in the static averaging regime and where the protein's fluorescence decay in its excited state is much shorter than its rotational rate. Thus, each eGFP separation and orientation per FRET pair would contribute as a single component within the time-resolved fluorescence anisotropy decay, yielding a multi-exponential decay.

The eGFPs are considered to be motionless during the time scale of the fluorescence decay, since the fluorescence lifetime of eGFP is much shorter (≈ 2.5 ns(11, 77–79), Table S1) than its rotational correlation time (≈ 15 ns in water(18, 36, 60, 79, 84–91),

Table S2). Therefore, the fluorescence anisotropy is assumed to be exclusively determined by the process of energy transfer. Because the sample consists of a diluted solution of eGFPs, we can model it as a spatially isotropic and disordered system. Moreover, the concentration of proteins is sufficiently low that the probability of multi-migration processes is negligible and all the pairwise interactions between the excited donor and acceptor are independent. In addition, the initially excited eGFP (donor) is considered to be the major contributor to the anisotropic response and a 3-dimensional solution was initially considered by setting $\delta = 1/2$ in equation 10(31, 32, 62, 63). This reduced the number of free fitting parameters to four, the same as for a single exponential anisotropy decay, equation 9. The fit of the eGFP dimer anisotropy data with the stretched exponential decay model yielded two fit parameters: r_0 and γ_{st}. The fit parameter γ_{st}, given by equation 30, decreased with the solution viscosity (Figure 6 f), while r_0 presented no correlation (not shown).

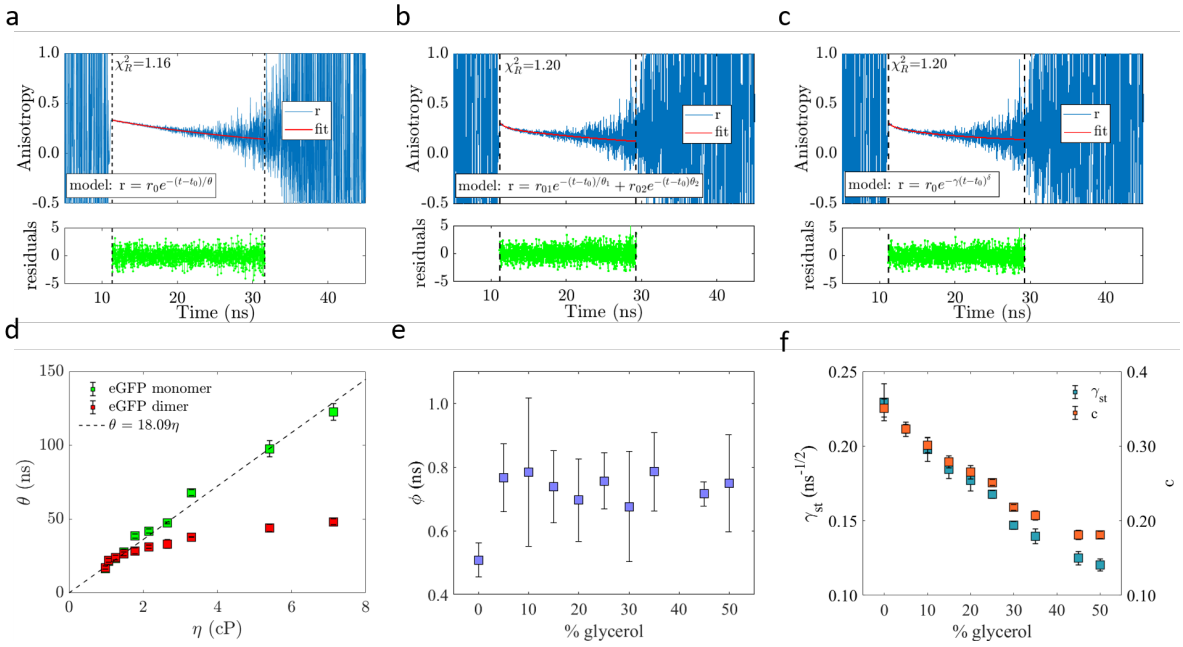

Figure 6: (a) Representative time-resolved fluorescence anisotropy decay, fit and residuals for the eGFP monomer. The equivalent time-resolved anisotropy decay corresponding to the eGFP dimer fitted with a (b) double and (c) stretched exponential decay model. The solvent is 10% glycerol and 90% PBS. (d) Rotational correlation time plotted against viscosity for monomer and dimer. The monomer data are fitted with a straight line passing through the origin according to equation 1, with a gradient of 18.1 ns/cP. This yields a hydrodynamic radius R_h for the monomer of $R_h = 2.46$ nm $\pm$ 0.01 nm. (e) FRET inverse rate ϕ and (f) γ_{st} and c parameters plotted against sample composition in % glycerol.

From equation 11, γ is expected to vary slightly with the refractive index of the solution, due to its dependence on the lifetime which is a function of the refractive index but not quite as much as we observe. According to theory, when the system is isotropic and 3-dimensional and behaves within a static regime, the orientational-factor $|\kappa|$ can be averaged to 0.69(63, 96) and is thus constant. The dimensionless parameter c should also be constant, but varies too, as shown in (Figure 6 f), with the difference between γ and c due to the refractive index effect on the average GFP lifetime. One possible explanation for the larger decrease of γ_{st} than expected, and the variation of c, could be related to a small contribution from Brownian rotational motion, which depolarises the emission and is not fully accounted for in the stretched exponential model. In the low viscosity region, depolarisation due to rotational motion will be added to depolarisation due to homo-FRET, and thus inflate these values. This is less of an effect in higher viscosity regimes.

In order to validate $\delta = 0.5$, the anisotropy data were also fitted with the stretched exponential decay model, letting δ be a floating fit parameter. Values of δ very close to 0.5 were found across all the varying viscosity solutions, see Figure 7 and Table S4, which confirms that considering the system as 3-dimensional is a sensible approach.

On an additional note, it is worth mentioning that the goodness of the stretched exponential decay fit given by χ^2_R was the same for the double exponential decay model, which has more fitting parameters, even when δ not fixed at 0.5 and is a floating fit parameter. Thus, the double exponential decay model is not a statistically justified model.

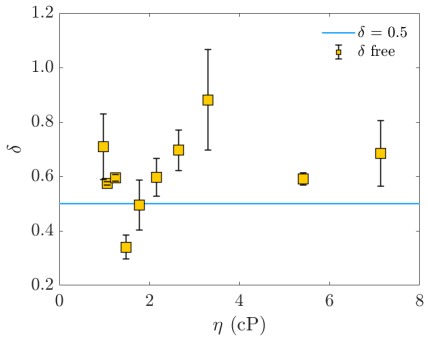

Figure 7: The dimensionality parameter δ from the stretched exponential decay model (equation 10), allowed to float freely in the fit, plotted against the solution viscosity. δ = 0.5, which indicates a 3-dimensional system, is given by the cyan continuous line.

Experimental E_{FRET} per eGFP dimer anisotropy model

FRET theory was applied to calculate the FRET efficiencies (equations 12 and 14), when the anisotropy data were interpreted via stretched exponential(31, 32) and double exponential(30) decay models. For this purpose, the experimental fluorescence lifetime τ of the single eGFP monomer was employed. Detailed data are given in Supplementary Material (Table S5).

Figure 8 a shows that the FRET efficiencies calculated from the double exponential decay model (equation 14) were located within a narrow range above 0.5 (between 0.617 ± 0.002 and 0.723 ± 0.001, in 50% glycerol solution and PBS, respectively). No correlation between FRET efficiencies and solution viscosities were encountered. This was an expected result since the fluorescence lifetime only varied by about 9% (between 2.65 ns ± 0.01 ns in PBS, and 2.41 ns ± 0.02 ns in 50% glycerol solution) across solutions (Table S5) and the FRET inverse rate ϕ showed no correlation with the solution viscosity (Figure 6).

The FRET efficiencies calculated from the stretched exponential decay model (equation 12) were below 0.5 (between 0.18 ± 0.01 and 0.32 ± 0.01, in 50% glycerol solution and PBS, respectively) and within a much wider range of values, presenting a correlation with the solution viscosity, in the same way as the γ_{st} parameter (higher values were associated with low viscous solutions and lower values with high viscous solutions) (Figure 8 b). As pointed out in the previous section, the γ_{st} parameter should remain largely unchanged, which would result in a narrower range of FRET efficiencies. However, residual Brownian motion may contribute to depolarisation which may inflate FRET efficiencies, particularly in the lower viscosity regime, and spread out the FRET efficiency range.

Since the distance between proteins and their relative orientations cannot be separated experimentally, molecular dynamics (MD) simulations were performed in order to investigate these parameters independently.

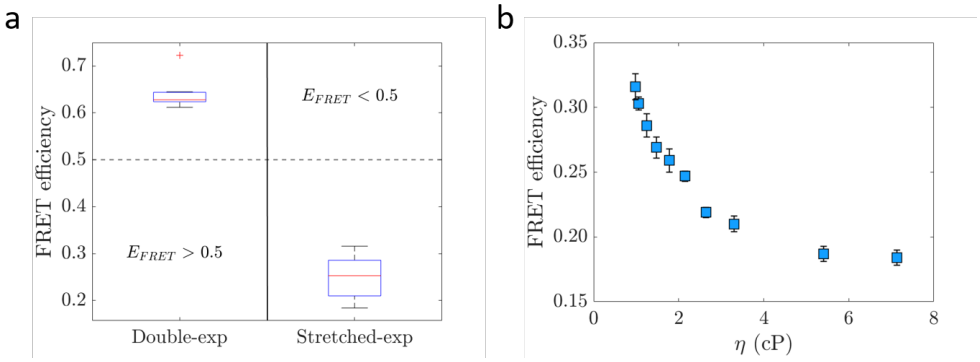

Figure 8: (a) Boxplots of the calculated FRET efficiencies between the two eGFPs of the dimer for each anisotropy decay model: double and stretched exponential. The horizontal red line in the boxplot corresponds to the median, and the bottom and top blue edges of the box correspond to the 25^{th} and 75^{th} percentiles. The whiskers extend to the most extreme data points not considered outliers, and the outliers are plotted individually using the '+' symbol. (b) Relationship between E_{FRET} and the solution viscosity.

Molecular dynamics simulations

Molecular dynamics simulations: orientational-factors

FRET efficiencies were calculated from the MD simulation trajectories (κ^2 and R), by combining equations 6 and 7, with $J(\lambda)$=8.7 × 10^{14} $M^{-1}cm^{-1}nm^4$, n = 1.336 and Φ = 0.6.

The distributions of R and κ^2 obtained from the last 450 ns of the MD simulations, are shown in Figure 9 a and b, respectively. In the inset plots, their temporal evolutions are shown, where the red dashed line indicates the starting point for collecting statistics for the corresponding distribution. R was approximately constant over time and a Gaussian fit of its distribution (red line) yielded $\langle R \rangle$ = 4.56 nm ± 0.07 nm (Figure 9 a). However, κ^2 presented an asymmetric and broad distribution, while its temporal evolution showed a well-defined and repetitive pattern (Figure 9 b). Because R is approximately constant, the variation in κ^2 is mirrored by the variation in E_{FRET} (Figure 9 c).

The κ^2 histogram shows a range of values between 0 and 0.9180, with a peak at κ^2 = 0, gradually dropping to zero for κ^2 = 1. κ^2 = 1 implies that the transition dipole moments of both monomers belong to parallel planes and are perpendicular to the vector that define their separation, $\vec{R}$. Since the transition dipole moment is defined within a plane perpendicular to the main axis of the GFP β-barrel (Figure 2), the two monomers would be perfectly stacked on top of each other. The rest of the κ^2 distribution ($0 \leq \kappa^2 < 1$) was due to tumbling and rotation around the previously described aligned orientation. Since most κ^2 values within this range were closer to 0 than to 1, the preferred configuration of the two GFPs was with the two transition dipole moments almost perpendicular to each other. For κ^2 between 0 and 1, two broad peaks can be observed around approximately 0.1 and 0.45. These populations are easier to discern in the FRET efficiency probability distribution, which extends from 0 to almost 0.6 (Figure 9 c). A rapid rotation took place in the first 50 ns, supported by the decrease on the fluorophore separation R, with a concomitant twist of the linker (Figure 9 a).

From the first 50 ns onward, the fluorophore separation remained approximately constant and α_T oscillated around the perpendicular configuration, α_T = 90° (Figure 9 d). Specifically, the probability distribution of the angle α_T was fitted with a double Gaussian-function, centred at 72° ± 8° (green line) and 94° ± 10° (black line), where a greater amount of events was found in the second peak. Additionally, a smooth tumbling and rotation were supported by the calculation of the angles α_D and α_A, whose values were in close proximity to 90°, either above (α_D) or below (α_A) this value (Figure 9 e and f). Like the α_T probability distribution, the correspondent to the angle α_D was fitted with a double Gaussian-function, with a second predominant peak of events. The two Gaussian functions were centred at 98° ± 4° (green line) and 108° ± 4° (black line). The angle α_A distribution was fitted with a single Gaussian-function, with μ and σ equal to 67° and 5°, respectively (red line). For the first two angular distributions (α_T and α_D), the convolution of the two Gaussian fit-functions is shown as a red envelope. To visualise the κ^2 and angular distributions analysis, a movie of the temporal evolution of the two GFPs tethered by the 15-aminoacids linker is available in the Supplementary Material, together with scatter plots showing the relative orientation of the two GFPs transition dipole moments (Figure S14).

The low magnitude of κ^2 (<0.8, Figure 9 b)) indicates that the two proteins arrange themselves such that they do not fully and homogeneously explore all possible orientations. This is not unexpected, as the linker restricts the full range of all possible orientations available to the two GFPs. The broad and asymmetric distributions of κ^2 and E_{FRET} have a large standard deviation in agreement with other work(97), which along with their mean values, were given by $\langle \kappa^2 \rangle$ = 0.17 ± 0.16 and $\langle E_{FRET} \rangle$ = 0.18 ± 0.14, respectively. Because the vast majority of the FRET efficiencies calculated from the MD simulations lie below 0.5, the results obtained from the stretched exponential decay model (equation 12) are in closer proximity to the MD simulations than the calculated ones via the double exponential decay model (equation 14) (Figure 8 a).

The κ distribution obtained from the simulations was calculated and is shown in Figure 10 a, where the inset plot corresponds to its temporal evolution over the duration of the simulation. The distribution was calculated from the data points after the dashed vertical red line at t = 50 ns. Equation 4 was employed to calculate κ, except for the square exponent. Three predominant populations of κ were discernible from its distribution from around -0.4 to 1.1. The most frequent values were at around 0.4 and formed the central peak of the distribution, with a smaller peak at 0.05, and a shoulder at 0.6. The majority of κ values were located above 0, with very few in the negative range of the distribution. Therefore, κ and $|\kappa|$ mean values are expected to be almost identical. The mean of the absolute value of κ was calculated, yielding $\langle |\kappa| \rangle$ = 0.35 ± 0.20. Since this result is well below the theoretical 0.69 for the static random averaging regime, (63, 96) this further shows that the two proteins are not exploring all the available 3-dimensional space, with the 15-aminoacid linker restricting their mobility.

Moreover, the distance from end to end of the linker was investigated over time. This is presented in Figure 10 b, where the data oscillates around a mean value of 1.45 nm ± 0.34 nm (red dashed line), from 0.49 nm and 2.59 nm (bottom and top green dashed lines). Since the linker is approximately 6 nm long when fully stretched, and the graph places its end-to-end mean value around 1.45 nm, the linker is significantly coiled. It seems reasonable to think that the flexibility of the linker is an intrinsic property of itself, instead of considering any dependence with the viscosity of the medium. Thus, we assumed that the different orientations established by the two GFPs and given by the orientational factor κ^2 would be invariant in outcome but enriched

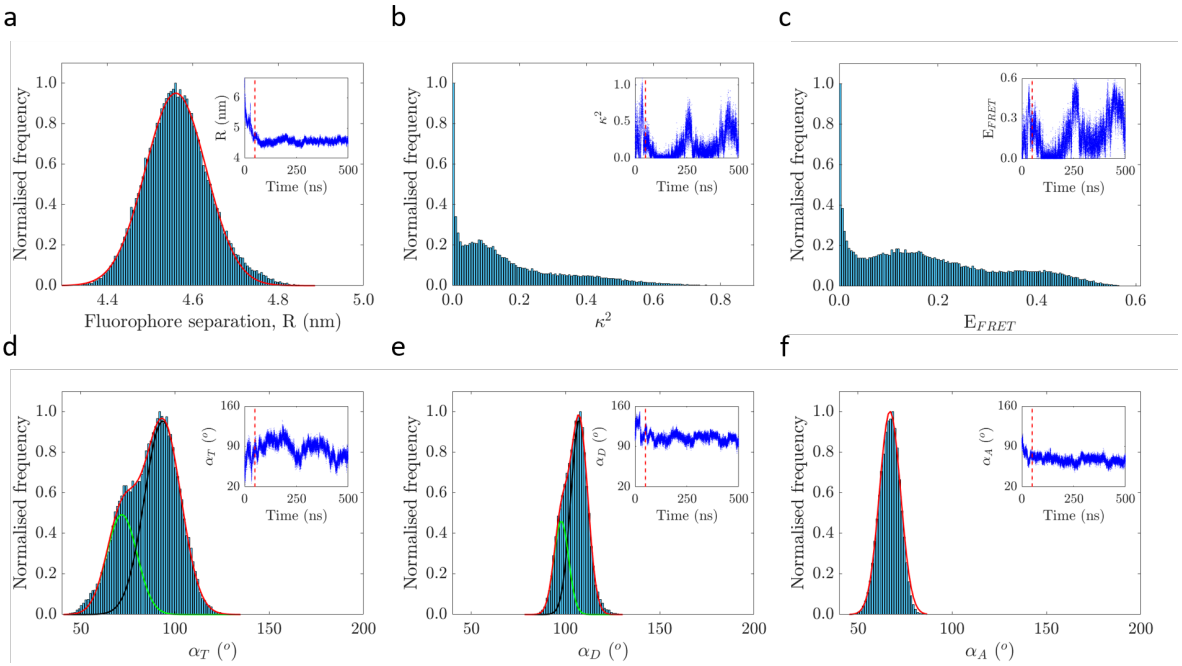

Figure 9: Distributions and temporal evolution (inset) from MD simulations with sampling every 10 ps of (a) fluorophore separation R, (b) relative dipole orientation κ^2 between GFP monomers, (c) FRET energy efficiency E_{FRET} calculated from equation 6 with R_0 = 4.65 nm, (d) angle between GFP monomers α_T, (e) angle between one GFP monomer and the vector $\vec{R}$, and (f) angle between the other GFP monomer and $\vec{R}$. Single and double-Gaussian functions were used to fit the separation and angular distributions, with further details given in the main text. Dashed vertical red lines shown in the inset plots define the starting point to generate the distributions.

from a statistical point of view with a decrease in the environmental viscosity, collecting the same κ^2 data in a shorter amount of time. Even if this was not the case, we would not be able to prove it experimentally due to the short fluorescence lifetime associated with these slow-motion fluorophores. Nonetheless, we believe that κ^2 should depend on the linker length rather than on the solution viscosity. A longer linker should confer a wider distance range on this FRET pair, and most likely also a wider κ^2 range. Conversely, some restriction of the linker may lead to a stronger restriction of the κ^2 orientations and thus to a more pronounced skewness of its distribution in comparison to randomly orientated GFPs(97).

It is worth mentioning, however, that a longer simulation time may in principle reveal a more complex behaviour of the linker. By construction, the configurations characterised by a fully stretched linker would not be accessible due to its initial folding and the subsequent system solvation and unit cell definition, although they would be expected to be rare events. While we are not able to assess with certainty that no other metastable energetic minima could be observed at unexplored points in the space defined by κ^2 and R, the tendency of the linker to fold, that dragged the two monomers close to one another within the first 50 ns, allows us to reasonably assume that the configuration observed beyond 50 ns is the absolute energetic value.

Overall, under the assumption that the MD simulations represent the absolute energetic minimum in the space defined by the orientational angles α, orientational factor κ and the separation between the fluorophores $\vec{R}$, the system would be in a highly restricted static averaging regime. The agreement between anisotropy decay analysis based on the stretched exponential function and simulation may constitute an *a-posteriori* validation of the initial assumption.

Time-resolved anisotropy decays of GFP and GFP15GFP in water from molecular dynamics simulations

In order to assess the rotational mobility of the GFP monomer and the GFP15GFP dimer, individual auto-correlation curves - which represent fluorescence anisotropy decays - were generated every 50 ns with a time resolution of 10 ps according to equation 3, averaged and fitted. Figure 11 a shows nine individual anisotropy decays for the GFP monomer, from nine 50 ns time windows of the 500 ns simulation, and b and c correspond to nine anisotropy decays for each GFP in the GFP15GFP dimer. An average anisotropy decay for the GFP monomer is shown in panel d, and the equivalent for the dimer in e. Both average anisotropy decays were fitted under the assumption that the anisotropy depolarisation was strictly governed by the Brownian rotational motion, where no FRET was present.

For the GFP monomer, the average time-resolved anisotropy decay was very well fitted with a single exponential decay

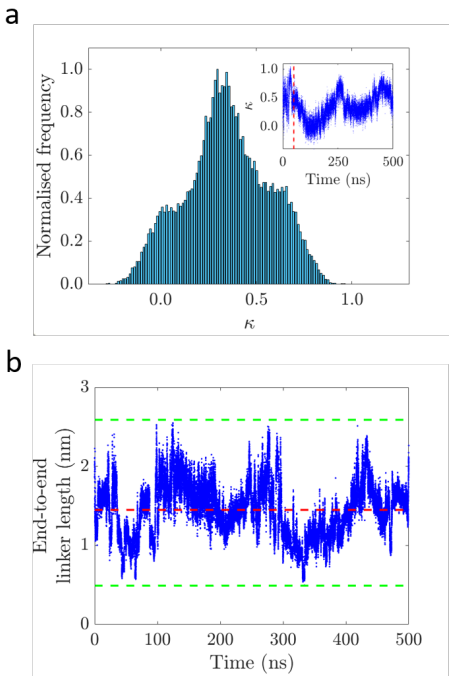

Figure 10: (a) Distribution and temporal evolution (inset) from MD simulations with 10 ps sampling of the orientational-factor κ. The dashed vertical red line in the inset indicates the start of the distribution. (b) Temporal evolution of the end-to-end linker length, where the horizontal dashed red line corresponds to the mean value (1.45 nm), and the bottom and top dashed green lines refer to the minimum and maximum values (0.49 nm and 2.59 nm, respectively).

model (Figure 11 d), which assumes that the protein is freely rotating and its shape can be modelled as a sphere. In order to assess how good this spherical approximation was, the anisotropy decay was also fitted with a double exponential decay model, giving rise to two identical rotational correlation times (not shown). This means that reducing the structure of GFP to a sphere is a valid approach. The rotational correlation time extracted from the single exponential decay fit was 4.60 ns ± 0.04 ns, with a goodness of fit of R^2=0.98. This low value for the rotational correlation time in comparison with the experimental rotational correlation time in Figure 6 d (16.5 ns ± 0.2 ns) is due to the TIP3P water model used in the MD simulations. In fact, the viscosity of TIP3P water is 0.321 cP at room temperature(51–53), considerably lower than the experimental water viscosity (1 cP). Although the experiments were measured in PBS buffer, its viscosity was considered to be identical to water(98, 99). With this information and applying the Stokes-Einstein-Debye equation (1), the actual rotational correlation time of the GFP monomer in water can be re-calculated by multiplying the result of the simulation by a scaling factor 1/0.321, which yields 14.3 ns ± 0.1 ns. This scaled value is in reasonable agreement with the experimentally measured rotational correlation time, θ = 16.5 ns ± 0.2 ns(18, 84–86).

For the GFP15GFP case, the data were initially fitted with a double exponential decay model, where one component presented a much longer rotational correlation time compared to the other. Then the contribution of this component was reduced to r_∞ yielding a hindered rotation model or the so-called wobble-in-a-cone model. The fit parameters and goodness of fit were found to be r_0 = 0.398 ± 0.001, r_∞ = 0.0604 ± 0.0003, θ = 9.62 ns ± 0.05 ns and R^2=0.98. $\frac{r_\infty}{r_0}$ = 0.152, and the interpretation of this model according to equation 19 is that each GFP wobbles around a common axis with a cone semi-angle of 59.03°(71, 72), while the entire entity (GFP15GFP) rotates slowly. The GFP dimer tumbling in such a restricted way is consistent with the narrow distribution of the orientational factor κ^2 in the FRET simulations, and is analogous to a fluorophore with restricted rotation in an ordered lipid bilayer(71). The scaled rotational correlation times of the two GFP constructs in PBS are: 30.0 ns and 14.3 ns, for dimer and monomer, respectively. These results confirm the GFP dimer rotates slower than the monomer and thus rules out the validity of the double exponential decay model to interpret the experimental time-resolved fluorescence anisotropy data.

In experiments, when the fluorescence lifetime of a large and thus slowly rotating protein is very short, the calculation of its rotational correlation time can be very challenging and inaccurate. This is why for large proteins, a probe with a longer fluorescence lifetime should be employed(100). We note that since MD simulations only account for dynamical properties via the autocorrelation in equation 3, and do not involve any fluorescence emission, there is no restriction coming from the

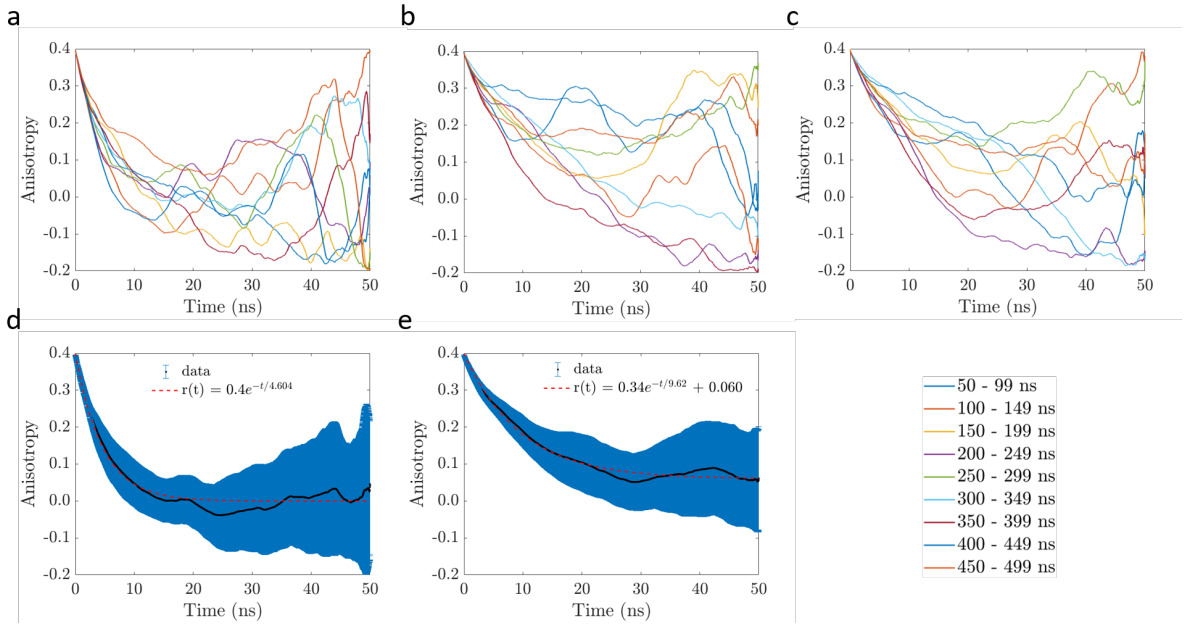

Figure 11: (a) Individual simulated anisotropy decays of the GFP monomer and (b,c) each GFP monomer of the GFP15GFP dimer, in water. (d) Average simulated anisotropy decay (solid black line) of the monomeric GFP, with fit (dashed red line). (e) Average simulated anisotropy decay of the GFP15GFP dimer with fit. The blue area of (d) and (e) are error bars that account for the calculated standard deviation per data point. The legend of the nine individual anisotropy decays from the 500 ns simulation of (a), (b) and (c) is located in the lower right corner.

fluorescence lifetime. In general, this allows the rotational correlation to be calculated independent of the fluorescence properties of the probe.

CONCLUSIONS

In the present work, we studied homo-FRET using a new homo-FRET standard, eGFP15eGFP, formed by two eGFPs tethered by a linker of 15 aminoacids (Figure 2). Steady-state anisotropy with red-edge excitation shows that homo-FRET occurs, and time-resolved fluorescence anisotropy experiments, analysed with a stretched exponential decay model, allow to calculate a FRET efficiency of around 25% for the construct. The fluorescence decays of both the GFP monomer and dimer are a function of the refractive index of their environment, as observed previously(11).

While in experimental FRET work, the distance and orientation of the fluorophores cannot be separated, MD simulations allow the distinction between distance and orientational contributions in the FRET efficiency. MD simulations revealed the distribution of the orientational factor κ via the angular distributions of the vectors separating the fluorophores (α_T, α_D and α_A, as defined in Figure 2), as shown in Figure 9 b, d, e and f. The two GFPs orientate themselves within a constrained frame, where tumbling and in-axis rotation of each individual GFP β-barrel equally contribute to the restricted range of orientational angles, and thus of κ and κ^2. The fluorophore distance does not show significant variations, see Figure 9 a, and together with κ^2, this allows us to calculate a FRET efficiency of $\langle E_{FRET} \rangle = 0.18 \pm 0.14$, from equation 6, which agrees well with the experimental data. Moreover, the autocorrelation of the tumbling motion enables us to calculate the equivalent of a fluorescence anisotropy decay, which also agrees well with the experimental data.

Thus, the combination of time-resolved fluorescence anisotropy and MD simulations allows us to gain detailed insight into the behaviour of the GFP dimer. We propose this construct as a homo-FRET standard, to be used for comparison with homo-FRET-based biosensors (101), and potentially as a reference when studying dimerisation processes in cells via FRET between GFP.

AUTHOR CONTRIBUTIONS

YTG and KS designed the research. YTG acquired the experimental data, while AC and CM designed and performed the MD simulations. AJB and RLB created the eGFP standards and helped with the design of the MD simulations. The experimental and simulated data were plotted and analysed by YTG, who also wrote this article. ALM helped with the experimental setup

and data analysis and JN critically reviewed and edited the published work. All authors reviewed the manuscript.

ACKNOWLEDGMENTS

YTG, ALM and AC would like to thank King's College London for funding of their Graduate Teaching Assistant PhD studentships. AC and CM are grateful for computational support from the UK high performance computing service ARCHER, for which access was obtained via the UKCP consortium and funded by EPSRC grant EP/P022472/1; they also acknowledge the UK Materials and Molecular Modelling Hub for computational resources, which is partially funded by EPSRC (EP/P020194/1). KS and JN acknowledge BBSRC grant BB/R004803/1.

REFERENCES

1. Tsien, R. Y., 1998. The green fluorescent protein. *Annual Review of Biochemistry* 67:509–544. https://doi.org/10.1146/annurev.biochem.67.1.509.

2. Ormö, M., A. B. Cubitt, K. Kallio, L. A. Gross, R. Y. Tsien, and S. J. Remington, 1996. Crystal structure of the aequorea victoria green fluorescent protein. *Science* 273:1392–1395. https://doi.org/10.1126/science.273.5280.1392.

3. Yang, F., L. G. Moss, and G. N. Phillips, 1996. The molecular structure of green fluorescent protein. *Nature Biotechnology* 14:1246–1251. https://doi.org/10.1038/nbt1096-1246.

4. Heim, R., D. C. Prasher, and R. Y. Tsien, 1994. Wavelength mutations and posttranslational autoxidation of green fluorescent protein. *Proceedings of the National Academy of Sciences* 91:12501–12504. https://doi.org/10.1073/pnas.91.26.12501.

5. Lossau, H., A. Kummer, R. Heinecke, F. Pöllinger-Dammer, C. Kompa, G. Bieser, T. Jonsson, C. Silva, M. Yang, D. Youvan, and M. Michel-Beyerle, 1996. Time-resolved spectroscopy of wild-type and mutant green fluorescent proteins reveals excited state deprotonation consistent with fluorophore-protein interactions. *Chemical Physics* 213:1 – 16. https://doi.org/10.1016/S0301-0104(96)00340-0.

6. Chattoraj, M., B. A. King, G. U. Bublitz, and S. G. Boxer, 1996. Ultra-fast excited state dynamics in green fluorescent protein: multiple states and proton transfer. *Proceedings of the National Academy of Sciences* 93:8362–8367. https://doi.org/10.1073/pnas.93.16.8362.

7. Haupts, U., S. Maiti, P. Schwille, and W. W. Webb, 1998. Dynamics of fluorescence fluctuations in green fluorescent protein observed by fluorescence correlation spectroscopy. *Proceedings of the National Academy of Sciences* 95:13573–13578. https://doi.org/10.1073/pnas.95.23.13573.

8. Creemers, T. M. H., A. J. Lock, V. Subramaniam, T. M. Jovin, and S. Völker, 2000. Photophysics and optical switching in green fluorescent protein mutants. *Proceedings of the National Academy of Sciences* 97:2974–2978. https://doi.org/10.1073/pnas.97.7.2974.

9. Weber, J. T., 2007. Green fluorescent protein: Properties, applications, and protocols. 2nd edition edited by M. Chalfie (Columbia University) and S. R. Kain (Agilent Technologies). Wiley-Interscience. *Journal of Natural Products* 70:141–141. https://doi.org/10.1021/np068247i.

10. Zimmer, M., 2002. Green fluorescent protein (GFP): Applications, structure, and related photophysical behavior. *Chemical Reviews* 102:759–782. https://doi.org/10.1021/cr010142r.

11. Suhling, K., J. Siegel, D. Phillips, P. M. French, S. Lévêque-Fort, S. E. Webb, and D. M. Davis, 2002. Imaging the environment of green fluorescent protein. *Biophysical Journal* 83:3589 – 3595. https://doi.org/10.1016/S0006-3495(02)75359-9.

12. Pliss, A., L. Zhao, T. Y. Ohulchanskyy, J. Qu, and P. N. Prasad, 2012. Fluorescence lifetime of fluorescent proteins as an intracellular environment probe sensing the cell cycle progression. *ACS Chemical Biology* 7:1385–1392. https://doi.org/10.1021/cb300065w.

13. Pliss, A., and P. N. Prasad, 2020. High resolution mapping of subcellular refractive index by fluorescence lifetime imaging: a next frontier in quantitative cell science? *Methods Appl. Fl.* 8:032001. https://doi.org/10.1088/2050-6120/ab8571.

14. Timpson, P., E. J. McGhee, J. P. Morton, A. Von Kriegsheim, J. P. Schwarz, S. A. Karim, B. Doyle, J. A. Quinn, N. O. Carragher, M. Edward, M. F. Olson, M. C. Frame, V. G. Brunton, O. J. Sansom, and K. I. Anderson, 2011. Spatial regulation of RhoA activity during pancreatic cancer cell invasion driven by mutant p53. *Cancer Research* 71:747–757. https://doi.org/10.1158/0008-5472.CAN-10-2267.

15. Miyawaki, A., J. Llopis, R. Heim, J. Michael McCaffery, J. A. Adams, M. Ikura, and R. Y. Tsien, 1997. Fluorescent indicators for Ca2+ based on green fluorescent proteins and calmodulin. *Nature* 388:882–887. https://doi.org/10.1038/42264.

16. Truong, K., A. Sawano, H. Mizuno, H. Hama, K. I. Tong, T. K. Mal, A. Miyawaki, and M. Ikura, 2001. FRET-based in vivo Ca2+ a imaging by a new calmodulin-GFP fusion molecule. *Nature Structural Biology* 8:1069–1073. https://doi.org/10.1038/nsb728.

17. Lakowicz, J. R., 2006. Principles of fluorescence spectroscopy. Springer.

18. Visser, A. J. W. G., A. H. Westphal, V. V. Skakun, and J. W. Borst, 2016. GFP as potential cellular viscosimeter. *Methods and Applications in Fluorescence* 4:035002. https://doi.org/10.1088%2F2050-6120%2F4%2F3%2F035002.

19. Clayton, A. H. A., Q. S. Hanley, D. J. Arndt-Jovin, V. Subramaniam, and T. M. Jovin, 2002. Dynamic fluorescence anisotropy imaging microscopy in the frequency domain (rFLIM). *Biophysical Journal* 83:1631–1649. https://doi.org/10.1016/S0006-3495(02)73932-5.

20. Patterson, P. D. W. . B. B. G., G. H., 2000. Förster distances between green fluorescent protein pairs. *Analytical Biochemistry* 284:438–440. https://doi.org/10.1006/abio.2000.4708.

21. Devauges, V., D. R. Matthews, J. Aluko, J. Nedbal, J. A. Levitt, S. P. Poland, O. Coban, G. Weitsman, J. Monypenny, T. Ng, and S. M. Ameer-Beg. Steady-state acceptor fluorescence anisotropy imaging under evanescent excitation for visualisation of FRET at the plasma membrane. *PLoS ONE* https://doi.org/10.1371/journal.pone.0110695.

22. Gautier, I., M. Tramier, C. Durieux, J. Coppey, R. B. Pansu, J. C. Nicolas, K. Kemnitz, and M. Coppey-Moisan, 2001. Homo-FRET microscopy in living cells to measure monomer-dimer transition of GFP-tagged proteins. *Biophysical Journal* 80:3000–3008. https://doi.org/10.1016/S0006-3495(01)76265-0.

23. Varma, R., and S. Mayor, 1998. GPI-anchored proteins are organized in submicron domains at the cell surface. *Nature* 394:798–801. https://doi.org/10.1038/29563.

24. Matthews, D. R., G. O. Fruhwirth, G. Weitsman, L. M. Carlin, E. Ofo, M. Keppler, P. R. Barber, I. D. Tullis, B. Vojnovic, T. Ng, and S. M. Ameer-Beg, 2012. A multi-functional imaging approach to high-content protein interaction screening. *PLoS ONE* 7. https://doi.org/10.1371/journal.pone.0033231.

25. Koushik, S. V., H. Chen, C. Thaler, H. L. P. Iii, and S. S. Vogel, 2006. Cerulean , Venus , and Venus Y67C FRET Reference Standards. *Biophysical Journal* 99–101. https://doi.org/10.1529/biophysj.106.096206.

26. Pelet, S. B., M. J. R. Previte, and P. T. C. So, 2006. Comparing the quantification of Förster resonance energy transfer measurement accuracies based on intensity, spectral, and lifetime imaging. *Journal of Biomedical Optics* 11:1 – 11. https://doi.org/10.1117/1.2203664.

27. Nguyen, T. A., P. Sarkar, J. V. Veetil, S. V. Koushik, and S. S. Vogel, 2012. Fluorescence polarization and fluctuation analysis monitors subunit proximity, stoichiometry, and protein complex hydrodynamics. *PLoS ONE* 7:1–13. https://doi.org/10.1371/journal.pone.0038209.

28. Levitt, J. A., P. E. Morton, G. O. Fruhwirth, G. Santis, P.-H. Chung, M. Parsons, and K. Suhling, 2015. Simultaneous FRAP, FLIM and FAIM for measurements of protein mobility and interaction in living cells. *Biomedical Optics Express* 6:3842–3854. https://doi.org/10.1364/BOE.6.003842.

29. Altman, D., D. Goswami, T. Hasson, J. A. Spudich, and S. Mayor, 2007. Precise positioning of myosin VI on endocytic vesicles in vivo. *PLoS Biology* 5:1712–1722. https://doi.org/10.1371/journal.pbio.0050210.

30. Warren, S. C., A. Margineanu, M. Katan, C. Dunsby, and P. M. W. French, 2015. Homo-FRET based biosensors and their application to multiplexed imaging of signalling events in live cells. *International Journal of Molecular Sciences* 16:14695–14716. https://doi.org/10.3390/ijms160714695.

31. Novikov, E. G., A. van Hoek, A. J. W. G. Visser, and J. W. Hofstraat, 1999. Linear algorithms for stretched exponential decay analysis. *Optics Communications* 166:189–198. https://doi.org/10.1016/S0030-4018(99)00262-X.

32. Bodunov, E. N., and M. N. Berberan-Santos, 2015. Stretched exponential kinetics of the luminescence concentration depolarization and penetration depth of molecules in a medium. *Optics and Spectroscopy (English translation of Optika i Spektroskopiya)* 119:22–28. https://doi.org/10.1134/S0030400X1507005X.

33. Studier, F. W., 2005. Protein production by auto-induction in high density shaking cultures. *Protein expression and purification* 41:207–234. https://doi.org/10.1016/j.pep.2005.01.016.

34. Chandrasekhar, S., 1943. Stochastic problems in physics and astronomy. *Rev. Mod. Phys.* 15:1–89. https://doi.org/10.1103/revmodphys.15.1.

35. Hertz, P., 1909. Über den gegenseitigen durchschnittlichen Abstand von Punkten, die mit bekannter mittlerer Dichte im Raume angeordnet sind. *Mathematische Annalen* 67:387–398. https://link.springer.com/article/10.1007%2FBF01450410.

36. Widengren, J., Ü. Mets, and R. Rigler, 1999. Photodynamic properties of green fluorescent proteins investigated by fluorescence correlation spectroscopy. *Chemical Physics* 250:171–186. https://doi.org/10.1016/S0301-0104(99)00255-4.

37. Levitt, J. A., P. Chung, M. K. Kuimova, G. Yahioglu, Y. Wang, J. Qu, and K. Suhling, 2011. Fluorescence anisotropy of molecular rotors. *ChemPhysChem* 12:662–672. https://doi.org/10.1002/cphc.201000782.

38. Søren Preus. a|e - UV-Vis-IR Spectral Software. www.fluortools.com.

39. Bashkatov, A. N., and E. A. Genina, 2003. Water refractive index in dependence on temperature and wavelength: a simple approximation. *In* V. V. Tuchin, editor, Saratov Fall Meeting 2002: Optical Technologies in Biophysics and Medicine IV. International Society for Optics and Photonics, SPIE, volume 5068, 393 – 395. https://doi.org/10.1117/12.518857.

40. Royant, A., and M. Noirclerc-Savoye, 2011. Stabilizing role of glutamic acid 222 in the structure of enhanced green fluorescent protein. *Journal of Structural Biology* 174:385 – 390. https://doi.org/10.1016/j.jsb.2011.02.004.

41. Land, H., and M. S. Humble, 2018. YASARA: A tool to obtain structural guidance in biocatalytic investigations, Springer New York, 43–67. https://doi.org/10.1007/978-1-4939-7366-8_4.

42. Guex, N., M. C. Peitsch, and T. Schwede, 2009. Automated comparative protein structure modeling with SWISS-MODEL and Swiss-PdbViewer: A historical perspective. *Electrophoresis* 30:S162–S173. https://doi.org/10.1002/elps.200900140.

43. Biasini, M., P. Benkert, and T. Schwede, 2010. Toward the estimation of the absolute quality of individual protein structure models. *Bioinformatics* 27:343–350. https://doi.org/10.1093/bioinformatics/btq662.

44. Waterhouse, A., G. Studer, G. Tauriello, L. Bordoli, S. Bienert, T. de Beer, and T. Schwede, 2016. The SWISS-MODEL Repository—new features and functionality. *Nucleic Acids Research* 45:D313–D319. https://doi.org/10.1093/nar/gkw1132.

45. Bertoni, M., , F. Kiefer, M. Biasini, L. Bordoli, and T. Schwede, 2017. Modeling protein quaternary structure of homo- and hetero-oligomers beyond binary interactions by homology. *Scientific Reports* 7:10480. https://doi.org/10.1038/s41598-017-09654-8.

46. Waterhouse, A., C. Rempfer, F. T. Heer, G. Studer, G. Tauriello, L. Bordoli, M. Bertoni, R. Gumienny, R. Lepore, S. Bienert, T. A. de Beer, and T. Schwede, 2018. SWISS-MODEL: homology modelling of protein structures and complexes. *Nucleic Acids Research* 46:W296–W303. https://doi.org/10.1093/nar/gky427.

47. Maier, J. A., C. Martinez, K. Kasavajhala, L. Wickstrom, K. Hauser, and C. Simmerling, 2015. ff14SB: Improving the accuracy of protein side chain and backbone parameters from ff99SB. *Journal of Chemical Theory and Computation* 11:3696–3713. https://doi.org/10.1021/acs.jctc.5b00255.

48. Bayly, C. I., P. Cieplak, W. Cornell, and P. A. Kollman, 1993. A well-behaved electrostatic potential based method using charge restraints for deriving atomic charges: the RESP model. *The Journal of Physical Chemistry* 97:10269–10280. https://doi.org/10.1021/j100142a004.

49. Jakalian, A., B. L. Bush, D. B. Jack, and C. I. Bayly, 2000. Fast, efficient generation of high-quality atomic charges. AM1-BCC model: I. Method. *Journal of Computational Chemistry* 21:132–146. https://doi.org/10.1002/(sici)1096-987x(20000130)21:2<132::aid-jcc5>3.0.co;2-p.

50. Mancini, O., T. Wellbrock, O. J. Rolinski, K. Kubiak-Ossowska, and P. A. Mulheran, 2018. Probing beta amyloid aggregation using fluorescence anisotropy : Experiments and simulation. *Physical Chemistry Chemical Physics* 20:4216–4225. https://doi.org/10.1039/C7CP08217G.

51. Jorgensen, W. L., J. Chandrasekhar, J. D. Madura, R. W. Impey, and M. L. Klein, 1983. Comparison of simple potential functions for simulating liquid water. *The Journal of Chemical Physics* 79:926–935. https://doi.org/10.1063/1.445869.

52. González, M. A., and J. L. F. Abascal, 2010. The shear viscosity of rigid water models. *The Journal of Chemical Physics* 132:096101. https://doi.org/10.1063/1.3330544.

53. Song, Y., and L. L. Dai, 2010. The shear viscosities of common water models by non-equilibrium molecular dynamics simulations. *Molecular Simulation* 36:560–567. https://doi.org/10.1080/08927021003720553.

54. Salomon-Ferrer, R., D. A. Case, and R. C. Walker, 2013. An overview of the Amber biomolecular simulation package. *WIREs Computational Molecular Science* 3:198–210. https://www.onlinelibrary.wiley.com/doi/abs/10.1002/wcms.1121.

55. Berendsen, H. J. C., J. P. M. Postma, W. F. van Gunsteren, A. DiNola, and J. R. Haak, 1984. Molecular dynamics with coupling to an external bath. *The Journal of Chemical Physics* 81:3684–3690. https://doi.org/10.1063/1.448118.

56. Lipari, G., and A. Szabo, 1980. Effect of librational motion on fluorescence depolarization and nuclear magnetic resonance relaxation in macromolecules and membranes. *Biophysical Journal* 30:489 – 506. https://doi.org/10.1016/S0006-3495(80)85109-5.

57. Schröder, G. F., U. Alexiev, and H. Grubmüller, 2005. Simulation of fluorescence anisotropy experiments: probing protein dynamics. *Biophysical Journal* 89:3757 – 3770. https://doi.org/10.1529/biophysj.105.069500.

58. Košovan, P., Z. Limpouchová, and K. Procházka, 2006. Molecular dynamics simulation of time-resolved fluorescence anisotropy decays from labeled polyelectrolyte chains. *Macromolecules* 39:3458–3465. https://doi.org/10.1021/ma052557a.

59. Best, R., H. Hofmann, D. Nettels, and B. Schuler, 2015. Quantitative Interpretation of FRET experiments via molecular simulation: force field and validation. *Biophysical Journal* 108:2721 – 2731. https://doi.org/10.1016/j.bpj.2015.04.038.

60. Hunt, J., A. H. Keeble, R. E. Dale, M. K. Corbett, R. L. Beavil, J. Levitt, M. J. Swann, K. Suhling, S. Ameer-Beg, B. J. Sutton, and A. J. Beavil, 2012. A fluorescent biosensor reveals conformational changes in human immunoglobulin E Fc: implications for mechanisms of receptor binding, inhibition, and allergen recognition. *Journal of Biological Chemistry* 287:17459–17470. https://doi.org/10.1074/jbc.M111.331967.

61. Wan, S., S. Liu, G. Zhao, M. Chen, K. Han, and M. Sun, 2007. Photoabsorption of green and red fluorescent protein chromophore anions in vacuo. *Biophysical Chemistry* 129:218 – 223. https://doi.org/10.1016/j.bpc.2007.06.003.

62. Huber, D. L., D. S. Hamilton, and B. Barnett, 1977. Time-dependent effects in fluorescent line narrowing. *Physical Review B* 16:4642–4650. https://doi.org/10.1103/PhysRevB.16.4642.

63. Baumann, J., and M. D. Fayer, 1986. Excitation transfer in disordered two-dimensional and anisotropic three-dimensional systems: effects of spatial geometry on time-resolved observables. *The Journal of Chemical Physics* 85:4087–4107. https://doi.org/10.1063/1.450880.

64. Förster, T., 1949. Experimentelle und theoretische Untersuchung des zwischenmolekularen Übergangs von Elektronenanregungsenergie. *Zeitschrift fur Naturforschung - Section A Journal of Physical Sciences* 4:321–327. https://doi.org/10.1515/zna-1949-0501.

65. Förster, T., 1959. 10th Spiers Memorial Lecture. Transfer mechanisms of electronic excitation. *Discuss. Faraday Soc.* 27:7–17. https://doi.org/10.1039/DF9592700007.

66. Berberan-Santos, M. N., and B. Valeur, 1991. Fluorescence depolarization by electronic energy transfer in donor–acceptor pairs of like and unlike chromophores. *The Journal of Chemical Physics* 95:8048–8055. https://doi.org/10.1063/1.461285.

67. Becker, W., 2005. Advanced time-correlated single photon counting techniques. Springer-Verlag Berlin Heidelberg, 1 edition.

68. Sillen, A., and Y. Engelborghs, 1998. The correct use of "average" fluorescence parameters. *Photochemistry and Photobiology* 67:475–486. https://doi.org/10.1111/j.1751-1097.1998.tb09082.x.

69. Strickler, S. J., and R. A. Berg, 1962. Relationship between absorption intensity and fluorescence lifetime of molecules. *The Journal of Chemical Physics* 37:814–822. https://doi.org/10.1063/1.1733166.

70. Cheng, N.-S., 2008. Formula for the viscosity of a glycerol-water mixture. *Industrial & Engineering Chemistry Research* 47:3285–3288. https://doi.org/10.1021/ie071349z.

71. Kinosita, K., S. Kawato, and A. Ikegami, 1977. A theory of fluorescence polarization decay in membranes. *Biophysical Journal* 20:289 – 305. https://doi.org/10.1016/S0006-3495(77)85550-1.

72. Heyn, M. P., 1979. Determination of lipid order parameters and rotational correlation times from fluorescence depolarization experiments. *FEBS Letters* 108:359–364. https://doi.org/10.1016/0014-5793(79)80564-5.

73. Michaud-Agrawal, N., E. J. Denning, T. B. Woolf, and O. Beckstein, 2011. MDAnalysis: a toolkit for the analysis of molecular dynamics simulations. *Journal of Computational Chemistry* 32:2319–2327. https://doi.org/10.1002/jcc.21787.

74. Gowers, R. J., M. Linke, J. Barnoud, T. J. E. Reddy, M. N. Melo, S. L. Seyler, D. L. Dotson, J. Domanski, S. Buchoux, I. M. Kenney, , and O. Beckstein, 2016. MDAnalysis: A Python package for the rapid analysis of molecular dynamics simulations. *Proceedings of the 15th Python in Science Conference* 98–105. https://doi.org/10.25080/Majora-629e541a-00e.

75. Roe, D. R., and T. E. Cheatham, 2013. PTRAJ and CPPTRAJ: software for processing and analysis of molecular dynamics trajectory data. *Journal of Chemical Theory and Computation* 9:3084–3095. https://doi.org/10.1021/ct400341p.

76. Humphrey, W., A. Dalke, and K. Schulten, 1996. VMD - visual molecular dynamics. *Journal of Molecular Graphics* 14:33–38. https://doi.org/10.1016/0263-7855(96)00018-5.

77. Striker, G., V. Subramaniam, C. A. M. Seidel, and A. Volkmer, 1999. Photochromicity and fluorescence lifetimes of green fluorescent protein. *Journal of Physical Chemistry B* 8612–8617. https://doi.org/10.1021/jp991425e.

78. Cotlet, M., J. Hofkens, M. Maus, T. Gensch, M. Van der Auweraer, J. Michiels, G. Dirix, M. Van Guyse, J. Vanderleyden, A. J. W. G. Visser, and F. C. De Schryver, 2001. Excited-state dynamics in the enhanced green fluorescent protein mutant probed by picosecond time-resolved single photon counting spectroscopy. *The Journal of Physical Chemistry B* 105:4999–5006. https://doi.org/10.1021/jp003813i.

79. Heikal, A., S. Hess, and W. Webb, 2001. Multiphoton molecular spectroscopy and excited-state dynamics of enhanced green fluorescent protein (EGFP): acid-base specificity. *Chemical Physics* 274:37–55. https://doi.org/10.1016/S0301-0104(01)00486-4, cited By 109.

80. Toptygin, D., 2003. Effects of the Solvent Refractive Index and Its Dispersion on the Radiative Decay Rate and Extinction Coefficient of a Fluorescent Solute. *Journal of Fluorescence* 13:201–219. https://doi.org/10.1023/A:1025033731377.

81. van Manen, H.-J., Verkuijlen, Paul, P. Wittendorp, V. Subramaniam, T. K. van den Berg, D. Roos, and C. Otto, 2008. Refractive index sensing of green fluorescent proteins in living cells using fluorescence lifetime imaging microscopy. *Biophysical Journal* 94:L67–L69. https://doi.org/10.1529/biophysj.107.127837.

82. Davidson, N. M., P. J. Gallimore, B. Bateman, A. D. Ward, S. W. Botchway, M. Kalberer, M. K. Kuimova, and F. D. Pope, 2020. Measurement of the fluorescence lifetime of GFP in high refractive index levitated droplets using FLIM. *Phys. Chem. Chem. Phys.* 22:14704–14711. https://doi.org/10.1039/C9CP06395A.

83. Toptygin, D., R. S. Savtchenko, N. D. Meadow, S. Roseman, and L. Brand, 2002. Effect of the Solvent Refractive Index on the Excited-State Lifetime of a Single Tryptophan Residue in a Protein. *The Journal of Physical Chemistry B* 106:3724–3734. https://doi.org/10.1021/jp0133889.

84. Swaminathan, R., C. P. Hoang, and A. S. Verkman, 1997. Photobleaching recovery and anisotropy decay of green fluorescent protein GFP-S65T in solution and cells: cytoplasmic viscosity probed by green fluorescent protein translational and rotational diffusion. *Biophysical Journal* 72:1900–1907. https://doi.org/10.1016/S0006-3495(97)78835-0.

85. Partikian, A., B. Ölveczky, R. Swaminathan, Y. Li, and A. S. Verkman, 1998. Rapid diffusion of green fluorescent protein in the mitochondrial matrix. *Journal of Cell Biology* 140:821–829. https://doi.org/10.1083/jcb.140.4.821.

86. Novikov, E., V. Skakun, J. Borst, and A. Visser, 2018. Maximum entropy analysis of polarized fluorescence decay of (E)GFP in aqueous solution. *Methods and Applications in Fluorescence* 6. https://doi.org/10.1088/2050-6120/aa898b.

87. Hess, S. T., E. D. Sheets, A. Wagenknecht-Wiesner, and A. A. Heikal, 2003. Quantitative analysis of the fluorescence properties of intrinsically fluorescent proteins in living cells. *Biophysical Journal* 85:2566–2580. https://doi.org/10.1016/S0006-3495(03)74679-7.

88. Volkmer, A., V. Subramaniam, D. J. S. Birch, and T. M. Jovin, 2000. One- and two-photon excited fluorescence lifetimes and anisotropy decays of green fluorescent proteins. *Biophysical Journal* 78:1589–1598. https://doi.org/10.1016/S0006-3495(00)76711-7.

89. Uskova, M. A., J. W. Borst, M. A. Hink, A. Van Hoek, A. Schots, N. L. Klyachko, and A. J. Visser, 2000. Fluorescence dynamics of green fluorescent protein in AOT reversed micelles. *Biophysical Chemistry* 87:73–84. https://doi.org/10.1016/S0301-4622(00)00184-8.

90. Mullaney, J. M., R. B. Thompson, Z. Gryczynski, and L. W. Black, 2000. Green fluorescent protein as a probe of rotational mobility within bacteriophage T4. *Journal of Virological Methods* 88:35–40. https://doi.org/10.1016/S0166-0934(00)00166-X.

91. Suhling, K., D. M. Davis, and D. Phillips, 2002. The influence of solvent viscosity on the fluorescence decay and time-resolved anisotropy of green fluorescent protein. *Journal of Fluorescence* 12:91–95. https://doi.org/10.1023/a:1015323606154.

92. Terry, B. R., E. K. Matthews, and J. Haseloff, 1995. Molecular characterization of recombinant green fluorescent protein by fluorescence correlation microscopy. *Biochemical and Biophysical Research Communications* 217:21–27. https://doi.org/10.1006/bbrc.1995.2740.

93. Hink, M. A., R. A. Griep, J. W. Borst, A. van Hoek, M. H. M. Eppink, A. Schots, and A. J. W. G. Visser, 2000. Structural dynamics of green fluorescent protein alone and fused with a single chain Fv protein. *Journal of Biological Chemistry* 275:17556–17560. https://doi.org/10.1074/jbc.M001348200.

94. Bhunia, D., R. Chowdhury, K. Bhattacharyya, and S. Ghosh, 2015. Fluorescence fluctuation of an antigen–antibody complex: circular dichroism, FCS and smFRET of enhanced GFP and its antibody. *Phys. Chem. Chem. Phys.* 17:25250–25259. https://doi.org/10.1039/C5CP04908C.

95. Lee, H. B., A. Cong, H. Leopold, M. Currie, A. J. Boersma, E. D. Sheets, and A. A. Heikal, 2018. Rotational and translational diffusion of size-dependent fluorescent probes in homogeneous and heterogeneous environments. *Physical Chemistry Chemical Physics* 20:24045–24057. https://doi.org/10.1039/C8CP03873B.

96. van der Meer, B. W., D. M. van der Meer, and S. S. Vogel, 2013. Optimizing the orientation factor kappa-squared for more accurate FRET measurements, John Wiley Sons, Ltd, chapter 4, 63–104. https://doi.org/10.1002/9783527656028.ch04.

97. Vogel, S. S., T. A. Nguyen, B. W. van der Meer, and P. S. Blank, 2012. The impact of heterogeneity and dark acceptor states on FRET: implications for Using fluorescent protein donors and acceptors. *PLoS ONE* 7:1–14. https://doi.org/10.1371/journal.pone.0049593.

98. Brown, P. H., A. Balbo, H. Zhao, C. Ebel, and P. Schuck, 2011. Density contrast sedimentation velocity for the determination of protein partial-specific volumes. *PLoS ONE* 6. https://doi.org/10.1371/journal.pone.0026221.

99. Momen-Heravi, F., L. Balaj, S. Alian, A. J. Trachtenberg, F. H. Hochberg, J. Skog, and W. P. Kuo, 2012. Impact of biofluid viscosity on size and sedimentation efficiency of the isolated microvesicles. *Frontiers in Physiology* 3:1–6. https://doi.org/10.3389/fphys.2012.00162.

100. Hirvonen, L. M., G. O. Fruhwirth, N. Srikantha, M. J. Barber, J. E. Neffendorf, K. Suhling, and T. L. Jackson, 2016. Hydrodynamic Radii of Ranibizumab, Aflibercept and Bevacizumab Measured by Time-Resolved Phosphorescence Anisotropy. *Pharm Res* 33:2025–2032. https://doi.org/10.1007/s11095-016-1940-2.

101. Miller, R. C., C. P. Aplin, T. M. Kay, R. Leighton, C. Libal, R. Simonet, A. Cembran, A. A. Heikal, A. J. Boersma, and E. D. Sheets, 2020. FRET Analysis of Ionic Strength Sensors in the Hofmeister Series of Salt Solutions Using Fluorescence Lifetime Measurements. *The Journal of Physical Chemistry B* 124:3447–3458. https://doi.org/10.1021/acs.jpcb.9b10498, pMID: 32267692.

102. VanDerMeer, B. W., 2020. Kappaphobia is the elephant in the fret room. *Methods and Applications in Fluorescence* 8:030401. https://doi.org/10.1088%2F2050-6120%2Fab8f87.

103. Peterson, K. A., M. B. Zimmt, S. Linse, R. P. Domingue, and M. D. Fayer, 1987. Quantitative determination of the radius of gyration of poly(methyl methacrylate) in the amorphous solid state by time-resolved fluorescence depolarization measurements of excitation transport. *Macromolecules* 20:168–175. https://doi.org/10.1021/ma00167a028.

SUPPLEMENTARY MATERIAL

Theoretical background of the stretched exponential decay model

Although the derivation of the stretched exponential decay model has been covered in the literature, we briefly outline it since the procedure gives insight into the modelling of the system.

In solutions with motionless fluorophores during their excited state ($\tau \ll \theta$), the fluorescence anisotropy depolarisation can be thought to be exclusively dependent on FRET, whose rate decreases when increasing the separation between fluorophores (31).

When the fluorophores are identical, in addition to direct excitation of the donor (initially excited fluorophore), there is also a probability of re-excitation of the donor by the acceptor. The initially excited fluorophore is known to be the major contributor to the fluorescence anisotropy, since the fluorescence emission of excited fluorophores due to FRET depolarises nearly completely. The probabilities of these events to happen and contribute to the fluorescence anisotropy depolarisation are determined by the probability H(t)(32). Thus, the fluorescence anisotropy takes the form:

$$r(t) = r_0 H(t) \tag{20}$$

where r_0 is the initial anisotropy at time t = 0. The probability H(t) was calculated applying the Huber-Hamilton-Barnett method(62). In order to determine it, one must start from the excitation probability of the initially excited fluorophore (donor) as a combination of rate equations:

$$\frac{dP_k(t)}{dt} = -\sum_l \omega(R)\big(P_k(t) - P_{k'}(t)\big) \tag{21}$$

where the radiative decay term given by the fluorescence lifetime τ is omitted from the right-hand side as the overall fluorescence lifetime remains invariant due to homo-FRET. $P_k(t)$ is the probability of the donor to be excited at time t and $P_{k'}(t)$ is the probability of an acceptor to be excited by the donor at time t. The term $\omega(R)$ refers to the transfer of energy among fluorophores (FRET rate constant), identical in both directions ($\omega(R)_{kk'} = \omega(R)_{k'k}$) and is given by the following expression:

$$\omega(R) = \frac{1}{\tau}\frac{3}{2}\kappa^2(\Omega)\left(\frac{R_0}{R}\right)^6 \tag{22}$$

where τ is the isolated donor fluorescence lifetime, R_0 corresponds to the Förster distance, distance at which the energy efficiency due to FRET is half, and $\kappa^2(\Omega)$ describes the dipole interaction between donor and acceptor as a function of their relative orientation.

The first term on the right-hand side of equation 21 describes the loss of non-radiative energy of the initially excited fluorophore (donor) via FRET. The second term describes the re-excitation of the initially excited fluorophore (donor) due to the back transfer from the acceptor(17, 62).

Let's now consider the case of a single donor and a single acceptor. The donor will be designated with the subscript 1 (k $\rightarrow$ 1, from equation 21) and the acceptor with the subscript 2 (k' $\rightarrow$ 2). Setting the initial conditions $P_1(0) = 1$ and $P_2(0) = 0$, equation 21 can be solved for both fluorophores (donor and acceptor). The solution for the donor, which is the one we are interested in, is as follows:

$$P_1(t) = \frac{1}{2}\left(1 - e^{-2\omega(R)t}\right) \tag{23}$$

When the system consists of an array of fluorophores (donors and acceptors), the total fluorescence anisotropy will be given by all the donors' contributions. For this reason, the donor's excitation probability given by equation 23 must be expanded over the entire system, which gives rise to the configurational average H(t).

If the system is spatially conformed by an ordered array of fluorophores, such as a lattice, the transfer of energy will be identical everywhere. However, if this array is not ordered, the transfer of energy via FRET will depend on the local fluorophore concentrations and thus on the fluorophore separations. A spatial disorder, such as a diluted system, is modelled in such way that the donor occupies a central position at the origin and only independent pairwise interactions (donor and acceptor) are assumed to take place. If the fraction of sites occupied at random by fluorophores is given by p and the fraction of unoccupied sites as $1 - p$, then the configurational average $H(t)$ takes the following form(62, 63):

$$H(t) = \prod_{i=1}^{N}[pP_i(t) + (1-p)] = exp\Big(\sum_{i=1}^{N} ln[1 + p(P_i(t) - 1)]\Big) \tag{24}$$

where $P_i(t)$ corresponds to the i_{th} donor's excitation probability over the N lattice sites. This expression immediately implies that two fluorophores cannot occupy the same lattice site.

To indicate that the number of fluorophores within the lattice is low, the approximation $p \ll 1$ is introduced in equation 24. This approximation neglects the possibility of encountering two donors in the same neighbourhood. Thus, equation 24 can be rewritten as follows(62, 63):

$$H(t) \approx exp\Big(-p\sum_{i=1}^{N}(1 - P_i(t))\Big) \tag{25}$$

If we introduce the excitation probability of each individual donor $P_i(t)$ (equation 23) in equation 25, and the summation over sites is replaced by an integration over space, in a logarithmic scale, $H(t)$ takes the form(32, 63):

$$lnH(t) \approx -\frac{\rho}{2}\int_0^{\infty}\left(1 - e^{-2\omega(R)t}\right)u(R)dR \tag{26}$$

where the probability p becomes a number density ρ and $u(R)$ represents a continuous/uniform spatial distribution. In a 3-dimensional scenario $u(R) = 4\pi R^2$.

When the rotational rate of the fluorophore is much higher than the FRET rate between fluorophores, the fluorescence anisotropy of the overall system can still be assumed to decay only due to FRET. The fluorophores are still in the same position (no translational diffusion) and due to rapid rotation, the rotational correlation time θ is too small to be taken into account in the fluorescence anisotropy decay. In this case the system is said to be in the dynamic averaging regime and $\kappa^2(\Omega)$ can be averaged as follows(63, 96):

$$\langle\kappa^2\rangle = \int_{\Omega}\kappa^2(\Omega)\nu(\Omega)d\Omega \tag{27}$$

where $\nu(\Omega)$ is the angular distribution for an isotropic system(63).

Thus, $\kappa^2(\Omega)$ is replaced by $\langle\kappa^2\rangle$ in the transfer rate expression (equation 22). If we solve equation 26 for a 3-dimensional scenario and introduce in equation 20, the fluorescence anisotropy takes the following form:

$$r(t) = r_0 e^{-\frac{\rho}{2}\frac{4\pi\sqrt{\pi}}{3}\sqrt{\frac{2R_0^6 t}{\tau}}\left(\frac{3}{2}\right)^{1/2}\langle\kappa^2\rangle^{1/2}} \tag{28}$$

Now, let's define two new parameters, c and γ_d:

$$c = \frac{4\pi}{3}\rho R_0^3 \tag{29}$$

$$\gamma_d = \sqrt{\frac{\pi}{2\tau}}c\left(\frac{3}{2}\right)^{1/2}\langle\kappa^2\rangle^{1/2} \tag{30}$$

The dimensionless parameter c refers to the number of fluorophores within the 3-dimensional sphere volume of radius R_0.

Since we are describing a 3-dimensional isotropic system in the dynamic averaging regime, $\langle\kappa^2\rangle$ is replaced by 2/3(63, 96, 102). Thus γ_d turns into $\gamma_d = \sqrt{\frac{\pi}{2\tau}}c$. Introducing equations (29 and 30) in equation 28, the emission anisotropy is given as follows(31, 32, 103):

$$r(t) = r_0 e^{-\gamma_d t^{1/2}} \tag{31}$$

If we refer to the exponent of t in equation 31 as δ, we can see that for a 3-dimensional spatial distribution given by $u(R) = 4\pi R^2$, δ=1/2. If this distribution was assessed in a 2-dimensional scenario ($u(R) = 2\pi R$), δ would be equal to 1/3(31, 63).

In the previous analysis, the orientational factor κ^2 was averaged to 2/3 due to the rapid rotation of the fluorophore in comparison to its FRET rate constant. The system was said to be in the so-called dynamic averaging regime. However, when the fluorophores are strictly frozen during their fluorescence lifetime ($\tau \ll \theta$), the system is said to be in the static averaging regime. In this case, the orientational factor $\kappa^2(\Omega)$ has to be averaged over the angular distribution given by $\nu(\Omega)$ as follows(63):

$$lnH(t) \approx -\frac{\rho}{2}\int_0^\infty\int_\Omega\left(1 - e^{-2\frac{3}{2}\frac{1}{\tau}\left(\frac{R_0}{R}\right)^6\kappa^2(\Omega)t}\right)u(R)dR\nu(\Omega)d\Omega \tag{32}$$

Applying the same method as the applied for the dynamic averaging system, the fluorescence anisotropy takes the following form:

$$r(t) = r_0 e^{-\sqrt{\frac{\pi}{2}}c\left(\frac{3}{2}\right)^{1/2}\langle|\kappa|\rangle\left(\frac{t}{\tau}\right)^{1/2}} = r_0 e^{-\gamma_{st}t^{1/2}} \tag{33}$$

where:

$$\langle|\kappa|\rangle = \int_\Omega [\kappa^2(\Omega)]^{1/2}\nu(\Omega)d\Omega \tag{34}$$

and the new γ is:

$$\gamma_{st} = \sqrt{\frac{\pi}{2\tau}}c\left(\frac{3}{2}\right)^{1/2}\langle|\kappa|\rangle \tag{35}$$

Therefore, we see that the parameter γ in the dynamic and static averaging regimes differs in a scaling factor μ:

$$\mu = \frac{\gamma_{st}}{\gamma_d} = \frac{\langle|\kappa|\rangle}{\langle\kappa^2\rangle^{1/2}} \tag{36}$$

Thus, the fluorescence anisotropy of the system in the dynamic regime is dictated via γ by the orientational factor $\langle\kappa^2\rangle$, while $\langle|\kappa|\rangle$ dictates the fluorescence anisotropy decay of a static averaging system. We know that for a dynamic averaging 3-dimensional system, $\langle\kappa^2\rangle$ can be reduced to 2/3. In the static limit, when the system is isotropic and 3-dimensional, and the orientational factor describes a 3-dimensional distribution, $\langle|\kappa|\rangle$ can be calculated, yielding $\langle|\kappa|\rangle = 0.6901$. This is the same as saying that $\langle\sqrt{\kappa^2}\rangle^2 = 0.6901^2 = 0.4762$, with $\mu = 0.8452$. If the space is the same but the orientational factor describes a 2-dimensional distribution, then $\langle|\kappa|\rangle = 0.7397$, where $\langle\sqrt[3]{\kappa^2}\rangle^3 = 0.7397^3 = 0.4047$ and with $\mu = 0.8468$(63, 96).

An identical method to calculate the FRET efficiency of the entire system in either of the two regimes, dynamic or static, is now described. Let's define the fluorescence intensity decay of the contribution of all initially excited fluorophores (donors) in a system as follows:

$$I(t) = I_0 e^{-t/\tau}H(t) \tag{37}$$

where I_0 is the fluorescence intensity at $t = 0$ and τ is the fluorescence lifetime of the fluorophore. Because $H(t)$ does not take into account the finite fluorescence lifetime τ, an additional exponential term with the fluorescence lifetime is added in the equation. Since the initial excited fluorophores contribute predominantly to the fluorescence anisotropy, a relationship between their fluorescence steady-state anisotropy r and quantum yield Φ can be established(32):

$$\frac{r}{r_0} = \frac{\Phi}{\Phi_T} \tag{38}$$

where r_0 is the fluorescence anisotropy of the system in the absence of FRET and Φ_T is the total quantum yield.

If we consider the fluorescence intensity of the entire system $I_T(t)$ to decay as a single exponential function (an average fluorescence lifetime may be also introduced as an approximation), equation 38 takes the form(32, 65):

$$\frac{r}{r_0} = \frac{\Phi}{\Phi_T} = \frac{\int_0^\infty dtI(t)}{\int_0^\infty dtI_T(t)} = \frac{1}{\tau I_0}\int_0^\infty dtI(t) = \frac{1}{\tau}\int_0^\infty dte^{-t/\tau}H(t) \tag{39}$$

Introducing the explicit expression of the probability $H(t)$ within equation 39, the result is(32):

$$\frac{r}{r_0} = \frac{1}{\tau}\int_0^\infty dte^{-t/\tau}H(t) = 1 - f(y) \tag{40}$$

where

$$f(y) = \sqrt{\pi}ye^{y^2}[1 - erf(y)] \tag{41}$$

$$erf(y) = \frac{2}{\sqrt{\pi}}\int_0^y dte^{-t^2} \tag{42}$$

$$y = \frac{\sqrt{\tau}}{2}\gamma \tag{43}$$

The FRET efficiency of the donor fluorophores will be given by $f(y)$:

$$E_{FRET} = f(y) = \sqrt{\pi}ye^{y^2}[1 - erf(y)] \tag{44}$$

This expression (equation 44) is equivalent to $E_{FRET} = 1$ - Φ, where the quantum yield of the entire system is $\Phi_T = 1$.

Table S1: Fit parameters extracted from the fluorescence decays of a eGFP monomer and dimer (eGFP15eGFP) in solution. A double exponential decay model was used to fit the decays, measured with a single detector, according to equation 15 and the average fluorescence lifetime was calculated using equation 16. The average fluorescence lifetime and its reciprocal, per eGFP construct and refractive index solution n, are given by τ_{av} and τ_{av}^{-1}. The goodness of the fit is given by χ_R^2. The results are graphically shown in Figure 4 c.

			eGFP monomer			eGFP dimer		
% **glycerol**	**n ± 0.001**	**n^2 ± 0.001**	τ_{av} (ns)	χ_R^2	τ_{av}^{-1} (ns^{-1})	τ_{av} (ns)	χ_R^2	τ_{av}^{-1} (ns^{-1})
0	1.336	1.784	2.59 ± 0.02	1.34	0.386 ± 0.003	2.52 ± 0.06	1.42	0.396 ± 0.010
5	1.353	1.829	2.54 ± 0.01	1.34	0.394 ± 0.001	2.52 ± 0.01	1.26	0.398 ± 0.001
10	1.358	1.843	2.53 ± 0.01	1.30	0.395 ± 0.001	2.50 ± 0.01	1.42	0.401 ± 0.001
15	1.366	1.865	2.52 ± 0.02	1.29	0.396 ± 0.002	2.49 ± 0.02	1.08	0.402 ± 0.003
20	1.372	1.881	2.52 ± 0.01	1.25	0.398 ± 0.001	2.45 ± 0.02	1.28	0.408 ± 0.003
25	1.378	1.898	2.50 ± 0.01	1.26	0.401 ± 0.001	2.45 ± 0.01	1.17	0.409 ± 0.002
30	1.383	1.911	2.46 ± 0.01	1.17	0.407 ± 0.002	2.38 ± 0.04	1.19	0.420 ± 0.007

$\Delta n^2 = \sqrt{2n}\,\Delta n$

Presented errors are associated to standard deviations of average values

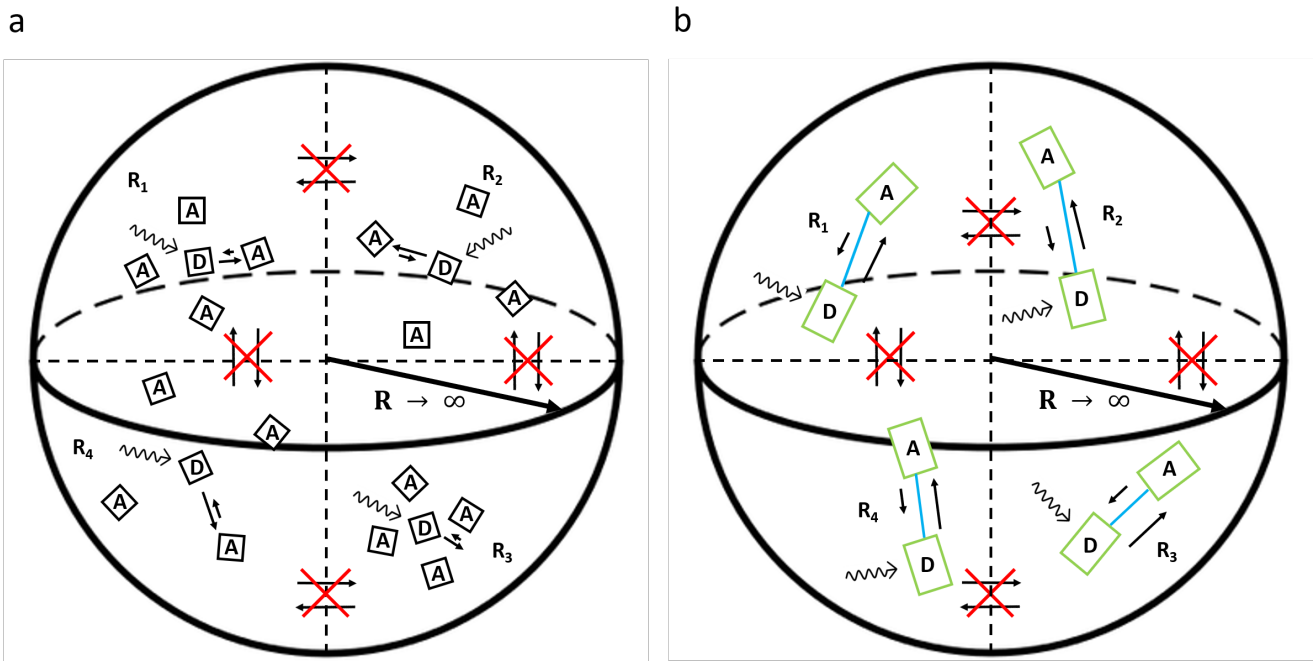

Figure S12: (a) Simplified graphical representation of the model described by Huber-Hamilton-Barnett(62) to quantify homo-FRET in a 3-dimensional diluted solution between identical fluorophores. The volume is divided in different regions determined by local concentrations and thus distances between fluorophores (R_1, R_2, R_3 and R_4). In each region a donor fluorophore is located in the middle and surrounded by acceptor fluorophores differently oriented. At time t a single interaction between donor and nearby acceptor takes place. The large arrow between donor and acceptor describes the transfer of energy via FRET from donor to acceptor. The short arrow represents the donor's re-excitation due to the transfer of energy via FRET from acceptor to donor. The pairs of arrows linking regions and crossed out in red represents the non-possibility of transferring energy via FRET between fluorophores of different regions. (b) Simplified graphical representation of the sample studied in this work, formed by a diluted solution of eGFP15eGFPs (two monomeric eGFPs (green) tethered by a linker of 15 aminoacids (blue)). This system corresponds to an analogy to (a), with the only difference that only two fluorophores (donor and acceptor at time t) are encountered for each region.

Table S2: Fit parameters derived from time-resolved fluorescence anisotropy measurements of a eGFP monomer in solution. A representative time-resolved fluorescence anisotropy decay along with the fit model are shown in Figure 6 a. The sample composition is given by its percentage of glycerol and viscosity η. The fit parameter r_0 corresponds to the initial anisotropy, θ is the rotational correlation time and the goodness of the fit is given by χ^2_R. The relationship between the rotational correlation time θ and the solution viscosity η is depicted in Figure 6 d in green square data points and a dashed black line, with a fit model whose gradient is 18.1 ns/cP.

% **glycerol**	η **(cP)**	r_0	θ **(ns)**	χ^2_R
0	0.98	0.322 ± 0.002	16.46 ± 0.20	1.15
5	1.06	0.337 ± 0.001	21.42 ± 0.42	1.18
10	1.25	0.331 ± 0.000	23.36 ± 0.26	1.20
15	1.48	0.335 ± 0.010	27.60 ± 2.00	1.17
20	1.78	0.334 ± 0.001	38.60 ± 1.34	1.11
25	2.15	0.342 ± 0.001	41.90 ± 1.46	1.13
30	2.65	0.343 ± 0.000	47.39 ± 0.55	1.17
35	3.30	0.327 ± 0.003	67.89 ± 2.00	1.12
45	5.41	0.346 ± 0.002	97.62 ± 5.55	1.13
50	7.13	0.342 ± 0.001	122.56 ± 5.52	1.19

Table S3: Fluorescence parameters extracted from the fit of time-resolved anisotropy measurements of a eGFP dimer in solution using a double exponential and a stretched exponential decay model. The fit parameters for the double exponential decay model (equation 13) are: rotational correlation time θ, the inverse FRET rate constant ϕ and initial anisotropy values associated with each exponential, r_{01} and r_{02}. Figure 6 d shows the dependence of the eGFP dimer rotational correlation time θ with the solution viscosity η (red square data points). The dependence of the inverse FRET rate constant ϕ on the viscosity η is shown in Figure 6 e. For the stretched exponential decay model (equation 10), the fit parameters are: the initial anisotropy r_0 and the static γ_{st} parameter found within the exponential. The dimensionality parameter δ was fixed at 0.5. The dimensionless parameter c was calculated from γ_{st} with $\langle|\kappa|\rangle$ = 0.69, and the goodness of both fits is indicated by χ^2_R. The dependence of γ_{st} and c on viscosity η is shown in Figure 6 f.

	Double exponential					Stretched exponential			
% glycerol	r_{01}	θ (ns)	r_{02}	ϕ (ns)	χ^2_R	r_0	γ_{st}	χ^2_R	c
0	0.254 ± 0.007	17.16 ± 1.06	0.047 ± 0.003	0.51 ± 0.05	1.15	0.311 ± 0.002	0.229 ± 0.012	1.17	0.351 ± 0.012
5	0.249 ± 0.004	22.12 ± 1.20	0.054 ± 0.000	0.77 ± 0.11	1.20	0.315 ± 0.005	0.211 ± 0.005	1.21	0.323 ± 0.006
10	0.254 ± 0.004	23.94 ± 1.63	0.054 ± 0.006	0.78 ± 0.23	1.20	0.316 ± 0.004	0.198 ± 0.008	1.22	0.301 ± 0.010
15	0.245 ± 0.002	26.35 ± 1.29	0.050 ± 0.006	0.74 ± 0.11	1.20	0.302 ± 0.003	0.185 ± 0.006	1.21	0.279 ± 0.008
20	0.253 ± 0.003	28.40 ± 2.08	0.053 ± 0.005	0.70 ± 0.13	1.15	0.310 ± 0.003	0.177 ± 0.007	1.17	0.265 ± 0.009
25	0.263 ± 0.001	31.30 ± 1.16	0.055 ± 0.004	0.76 ± 0.09	1.16	0.321 ± 0.002	0.168 ± 0.003	1.17	0.251 ± 0.004
30	0.269 ± 0.004	33.10 ± 2.99	0.045 ± 0.003	0.68 ± 0.17	1.12	0.317 ± 0.002	0.147 ± 0.003	1.14	0.218 ± 0.004
35	0.264 ± 0.001	37.86 ± 0.23	0.045 ± 0.002	0.78 ± 0.04	1.16	0.313 ± 0.004	0.140 ± 0.004	1.16	0.207 ± 0.006
45	0.267 ± 0.001	44.01 ± 2.37	0.044 ± 0.004	0.72 ± 0.04	1.14	0.313 ± 0.002	0.125 ± 0.004	1.18	0.181 ± 0.006
50	0.266 ± 0.000	48.15 ± 1.96	0.042 ± 0.003	0.75 ± 0.15	1.13	0.310 ± 0.002	0.120 ± 0.004	1.18	0.181 ± 0.005

Table S4: The dimensionality parameter δ from the stretched exponential decay model (equation 10) when allowed to float freely in the fit of the GFP dimer anisotropy decays.

% glycerol	η (cP)	δ
0	0.98	0.71 ± 0.12
5	1.06	0.58 ± 0.01
10	1.25	0.60 ± 0.01
15	1.48	0.34 ± 0.04
20	1.78	0.50 ± 0.10
25	2.15	0.60 ± 0.07
30	2.65	0.70 ± 0.07
35	3.30	0.88 ± 0.18
45	5.41	0.59 ± 0.02
50	7.13	0.69 ± 0.12

Table S5: FRET energy efficiency E_{FRET} of the eGFP dimer in solution and calculated from the fit parameters derived from time-resolved fluorescence anisotropy measurements. The double exponential decay model and stretched exponential decay models were applied. The fluorescence decays of the monomeric GFP were created from the parallel and perpendicular decays according to the denominator in equation 8. Equation 14 was applied to calculate the FRET efficiency when the anisotropy data was fitted with a double exponential decay model. For the stretched exponential decay model, E_{FRET} was calculated according to equation 12. The fluorescence lifetime of eGFP monomer in the absence of the acceptor is given by τ (equation 16). The results are presented graphically in Figure 8.

				Double exponential	Stretched exponential
% glycerol	η (cP)	n ± 0.001	τ (ns)	E_{FRET}	E_{FRET}
0	0.98	1.336	2.65 ± 0.01	0.723 ± 0.001	0.316 ± 0.010
5	1.06	1.353	2.63 ± 0.00	0.631 ± 0.000	0.303 ± 0.005
10	1.25	1.358	2.60 ± 0.00	0.624 ± 0.000	0.286 ± 0.009
15	1.48	1.366	2.56 ± 0.04	0.634 ± 0.003	0.269 ± 0.008
20	1.78	1.372	2.52 ± 0.02	0.644 ± 0.002	0.259 ± 0.009
25	2.15	1.378	2.51 ± 0.03	0.624 ± 0.003	0.247 ± 0.004
30	2.65	1.383	2.46 ± 0.02	0.645 ± 0.002	0.219 ± 0.004
35	3.30	1.389	2.47 ± 0.01	0.612 ± 0.001	0.210 ± 0.006
45	5.41	1.403	2.39 ± 0.01	0.625 ± 0.001	0.187 ± 0.006
50	7.13	1.407	2.41 ± 0.02	0.617 ± 0.002	0.184 ± 0.006

No error associated with viscosity η
Presented errors are associated with standard deviations of average values

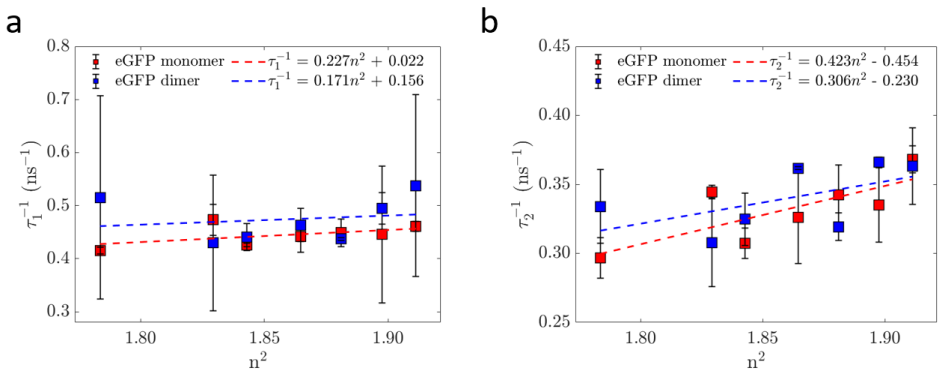

Figure S13: The short and long fluorescence lifetime of the GFP monomer and dimer from a double exponential fit to their fluorescence decays plotted versus the square of the refractive index. (a) Inverse of the shorter fluorescence lifetime plotted against the square of the refractive index. (b) Inverse of the longer fluorescence lifetime plotted against the square of the refractive index.

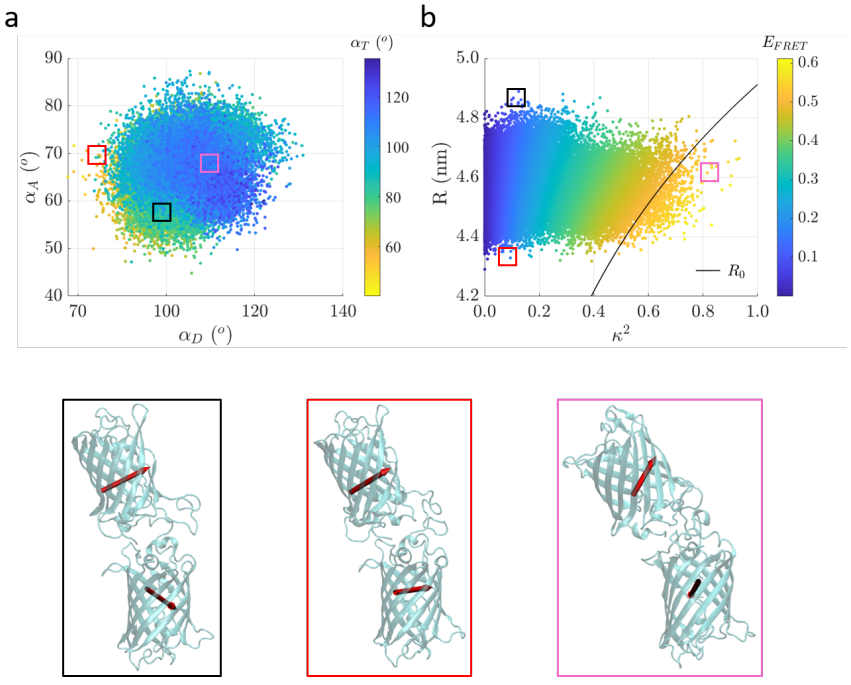

Figure S14: Scatter plots of (a) α_D, α_A and α_T, and (b) κ^2, fluorophore separation R and E_{FRET} of the GFP dimer (GFP15GFP). The GFP Förster distance R_0 as a function of κ^2 according to equation 7 is indicated by a line which follows the orange $E_{FRET} = 0.5$ shading. (c) Representative orientations of the two proteins from the differently coloured squares in the scatter plots in (a) and (b). The red arrows correspond to the GFP transition dipole moment $\vec{\mu}$, which indicates the fluorophore orientation of the protein.